X-RAY FLUORESCENCE MEASUREMENTS OF IRON IN THE SKIN USING A ^{109}CD-BASED SYSTEM

X-RAY FLUORESCENCE MEASUREMENTS OF IRON IN THE SKIN USING A ^{109}CD-BASED SYSTEM

By MICHELLE YAP, BSc

A Thesis Submitted to the Radiation Sciences Graduate Program and School of Graduate Studies in Partial Fulfillment of the Requirements for the Degree Master of Science

TITLE:	X-RAY FLUORESCENCE MEASUREMENTS OF IRON IN THE SKIN USING A ^{109}Cd-BASED SYSTEM
AUTHOR:	Michelle Yap BSc (Medical and Biological Physics Co-op), McMaster University, Hamilton, Canada
SUPERVISORS:	Dr. Michael Farquharson Dr. Fiona McNeill
COMMITTEE:	Dr. Bruce Wainman Dr. Michelle Zeller
NUMBER OF PAGES:	xv, 70

Lay Abstract

Iron deficiency and iron overload are common conditions that need to be addressed for overall patient health. There lacks a quick, non-invasive method of measuring iron to accurately monitor iron levels in the body.

The work in this thesis investigates the feasibility of a novel device that can measure iron in the body through the use of x-rays. The results of this study point towards the successful use of this device for iron measurements. Measurements of humans had results similar to previous measurements of iron phantoms and animal samples.

Further work is still required to determine the accuracy and validity of this system.

Abstract

Iron conditions can range from iron deficiency to iron overload. It is vital to accurately monitor iron levels so patients can receive proper treatment to reduce potential consequences such as organ failure. Current methods of measuring iron include blood tests and liver biopsies, both of which are invasive.

This work investigates the feasibility of using x-ray fluorescence (XRF) techniques to non-invasively measure iron in the body. The device employed for this work uses ^{109}Cd as the excitation source for XRF. Previously, this device had only been used to measure iron phantoms and ex vivo pig and rat skin samples. This thesis explores the use of this device for in vivo measurements.

Optimization and calibration of the device was completed to determine the optimal setup for in vivo measurements. A hand holder jig was designed and 3D-printed to secure participant hands for 1200-second measurements. 24 participants were recruited for this study who had no known iron diseases. 12 female and 12 male participants in the age range of 18 to 76 were measured. The average iron concentration was 9.1 ppm with a measurement uncertainty of 2.0 ppm. Importantly, the uncertainty in the in vivo measurements were similar to the uncertainty of phantom measurements, which suggests that human variations in hand size, position, and movement did not worsen measurement precision. No statistically significant differences were

observed across age and gender ($p>0.05$), suggesting that these factors do not affect measurement precision. Analysis of measurement uncertainties demonstrate that in vivo measurements are feasible with a 95% confidence level for measurements above 4.0 ppm.

This research points towards the feasibility of using this ^{109}Cd-based XRF device for in vivo measurements of iron. Further work is required to investigate the accuracy and validity of this device through comparison to currently accepted measurement methods.

This work is dedicated to my GonGon, Jimmy Chow

Acknowledgements

How can I ever fully thank everyone that has supported me along this journey? Primarily, I need to express my sincerest gratitude towards Mic and Fiona for being incredible mentors and guiding me along this stressful endeavour. Thank you for supporting me these past two years through all the ups and downs, and reassuring me when I felt like I was not doing well. I am especially grateful to Mic in my second year, for taking me on as a student during my undergraduate degree. Having the opportunity to continue the same work from undergrad for this master's thesis is a privilege I am lucky to have.

I am immensely thankful to my lab mates - Erica, Sami, and Laura - for showing me the ropes in the lab. Thank you for giving me great advice, and mentoring me through the tumultuous experience of graduate school. Thank you also to tech services - Jordan, Nick, and Mack - for being the engineers I am not! And an even bigger thank you to Justin for all his help in every area of his expertise (which is to say, a lot). Thank you to Sama for learning how to use a 3D printer for me! I owe the biggest thanks to Chris, who made the largest portion of this work possible.

To my office mates - Chloe, Helen, Shirlie, Jigar, Curtis, and Emily - thank you for all the laughs, coffee runs, and bets. You all remind me that while research is great, so is winning a bet and getting a free coffee from The Grind.

A huge thank you to my family - Mom, Dad, and Kevin - for getting me to where I am. I am so grateful for your unwavering support throughout my academic career despite the geographical distance between us. I am also so grateful to my PoPo, for believing in me always and wanting nothing but the best for me.

Finally, my eternal gratitude goes to Lukas. None of this work would be possible without your love and support (and your 3D-printer). You celebrate my wins, and help me find the good when I cannot see any. Everything I have accomplished is because of you. You are my sun and moon and stars.

Table of Contents

List of Figures

List of Tables

Definitions and Abbreviations

Definitions

Hotter/colder source

With respect to radiation, a hotter source is more radioactive, while a colder source is less radioactive.

Abbreviations

ID	Iron deficiency
IDA	Iron deficiency anaemia
RBC	Red blood cell
MRI	Magnetic resonance imaging
XRF	X-ray fluorescence
SDD	Silicon drift detector
HPGe	Hyper-pure germanium (detector)

Declaration of Academic Achievement

I declare that all the work presented in this thesis is my own work and does not involve any plagiarism or academic dishonesty.

I certify that I have read this thesis and that, in my opinion, it meets the requirements in both scope and quality as a dissertation for the degree of Master of Science.

Chapter 1

Introduction

1.1 Iron in the body

Iron is a vital element for the human body, used in important metabolic processes including DNA synthesis and the transport of oxygen in the blood [1]. In the body, iron is found bound to proteins such as haemoglobin and myoglobin. Iron is transported through the body bound to the protein transferrin [2]. Bone marrow incorporates iron into haemoglobin in erythrocytes for oxygen transport, which get broken down by macrophages, cycling through the plasma iron pool [3]. About 1-2 $mg \cdot d^{-1}$ of iron are absorbed by the intestine from dietary iron to compensate for the small amount of iron lost through exfoliation of epithelial cells [2]. Iron can also be lost through menstruation or other bleeding; however, the body has no means of actively excreting excess iron. Iron metabolism is thus regulated solely at the point of absorption [3]. The liver, spleen, and bone marrow are the main storage organs of iron, storing it as the insoluble protein ferritin in cells [2].

Serum ferritin levels can be measured to estimate the total amount of iron in the

body. Normal serum ferritin levels in men tend to range from 30-300 ng/mL, and 10-200 ng/mL in women [4]. Total body iron content can range from 1-5 g, with most iron stored in the liver [2, 3]. It is important to maintain iron homeostasis, as depleted or excess amounts of iron can be detrimental to the body. Iron diseases resulting in iron deficiency or iron overload have been observed, which are among the most common human diseases [5].

1.2 Iron conditions

Many iron diseases exist, resulting in conditions that range from iron deficiency to iron overload. The following section explores some of the diseases that can lead to either of these conditions.

1.2.1 Iron deficiency

Iron deficiency (ID) affects almost a quarter of the population worldwide [6]. ID is particularly prevalent in young children and premenopausal women, especially in low- and middle-income countries [7]. Because most iron absorption comes from diet, insufficient nutritional intake can result in depletion of iron stores. ID can also result from excessive blood loss, such as menstruation, or inadequate absorption, resulting from diseases such as celiac disease [7, 8]. Among post-menopausal women and men in high-income countries, digestive diseases are the most common cause of ID [8]. Severe ID can result in iron deficiency anaemia (IDA) when erythropoiesis, the production of red blood cells (RBCs), is inhibited [8].

Common symptoms of ID include fatigue, lethargy, pallor, and reduced concentration [7]. While the diagnosis of anaemia is determined by the World Health Organization to be a blood haemoglobin level below 130 g/L in men and 120 g/L in women, anaemia diagnoses do not give clear indication of an ID diagnosis [8]. Serum ferritin levels below 12 μg/L are widely accepted as an indication of depleted iron stores [4]. In Ontario, the lower limit of normal ferritin levels was raised to promote prompt treatment for ID and reduce risk of IDA [9]. Mild ID can be treated with oral iron supplementation. Parenteral iron therapy involves intravenous infusion of iron, which can be beneficial for patients with severe ID who have not responded to oral treatment [7].

1.2.2 Iron overload

Some iron diseases resulting in iron overload conditions include primary and secondary hemochromatosis. Primary hemochromatosis is a hereditary disease which is the most commonly inherited disease in North America [10]. A genetic mutation causes excess iron to be absorbed from the diet, leading to iron overload and an increase of iron in storage organs [11]. Secondary hemochromatosis occurs when iron overload results from reasons other than genetic conditions, such as treatment for other diseases. For example, patients suffering from anaemias such as β-thalassemia or sickle cell disease require blood transfusions to support their low levels of RBCs. A secondary consequence of the influx of RBCs during blood transfusions is an increase in systemic iron [12].

High levels of iron are associated with the production of free radicals which can lead to organ damage, especially in the liver, heart, and endocrine glands [3]. The

effects of iron toxicity become visible when damage has already resulted in liver cirrhosis, cardiomyopathy, or diabetes [13]. For this reason, treatment for iron overload diseases is vital. Phlebotomy is the most common treatment for primary hemochromatosis patients to maintain a normal amount of iron in the body [12]. Conversely, patients with secondary hemochromatosis are unable to participate in phlebotomy due to their preexisting anaemia conditions. Instead, iron chelation therapy is used, which removes excess stored iron [13].

1.3 Iron measurements in vivo

Many techniques can be employed to assess the amount of iron in vivo. Examples of measurements include blood tests for serum ferritin, liver biopsies, and magnetic resonance imaging (MRI).

1.3.1 Blood test

Serum ferritin levels can be assessed through a blood test. Other biochemical tests include evaluation of transferrin, transferrin saturation, and serum iron concentration [14]. Blood tests are beneficial for iron measurements as they are relatively inexpensive and readily available; however, blood tests do carry minimal risk due to their invasive nature.

Under standard conditions, serum ferritin correlates well with iron stored in the liver [15]. However, the presence of inflammation can severely increase serum levels of ferritin alongside other proteins. Cellular injury can also release excess ferritin [16]. Presence of these conditions unfortunately render measurements inaccurate.

1.3.2 Liver biopsy

Iron stores in the liver consistently increase alongside total body iron burden for some patients in iron overload conditions [17]. For this reason, direct measurement of hepatic iron concentration is the most specific and sensitive method to estimate total body iron burden [18]. Liver biopsies are thus largely considered the 'gold standard' for estimating iron levels under iron overload conditions.

As with any operation, however, liver biopsies carry risk. This procedure is invasive, introducing risk of complications such as infection or pneumothorax. Moreover, the mortality risk of a liver biopsy is 0.01% [19]. As a result, it can be difficult to use liver biopsies as a regular monitoring tool. Variability in iron concentrations from biopsies have also been observed, suggesting heterogeneity in iron distribution throughout the liver [20]. Iron level accuracy can thus be affected by the lobe of the liver that the sample is taken from.

1.3.3 Bone marrow biopsy

For patients with iron deficiency, bone marrow biopsies may be more suitable to measure iron levels. Iron stores in bone marrow will decrease before this effect is reflected in other areas such as haemoglobin, making it another reliable measure of iron levels [21].

However, as with liver biopsies, bone marrow biopsies are extremely invasive procedures which introduce additional risk. These samples tend to be taken from the sternum or posterior iliac crest [22]. Fatal complications from sternal puncture have been documented [22].

1.3.4 MRI

MRI is a non-invasive alternative way of measuring iron in vivo. The presence of iron as ferritin affects the relaxation time and susceptibility of tissue to the external magnetic field. MRI is advantageous as it images the entire liver, removing potential variability due to heterogeneity of iron distribution [23]. MRI has demonstrated sensitivity to iron levels, however only for iron overload diseases [17].

While feasible for measurements, MRI can be challenging to implement as a continuous monitoring tool. Scanner time and personnel can be costly, and access to an MRI machine can be limited in communities outside of urban centres [24].

1.4 X-ray fluorescence measurements

1.4.1 X-ray fluorescence

X-ray fluorescence (XRF) spectroscopy is a non-invasive technique that can be used to determine the elemental composition of a sample. When incident photons possess sufficient energy, they are able to interact with the inner-shell electron of an atom via photoelectric absorption. This creates a vacancy in the shell, which is filled by the transition of a higher-energy electron. As this higher-energy electron transitions, it can emit a photon or an Auger electron. A visualization of this process is shown in Figure 1.1. The energy of the emitted photon is equal to the difference in binding energy of the electron shells involved in the transition. Since these energy differences are unique to each atom, the emitted photons are characteristic and can be used to identify what elements are present in a sample, and the relative quantities.

Characteristic x-rays are categorized depending on the electronic transition which

occurred. For example, when an electron transitions from the L-shell to the K-shell, the emitted photon is called the K_α x-ray. In contrast, an electron transitioning from the M-shell to the K-shell is called the K_β x-ray. In much of this work, the K_α transition of iron is measured, which has an energy of 6.4keV.

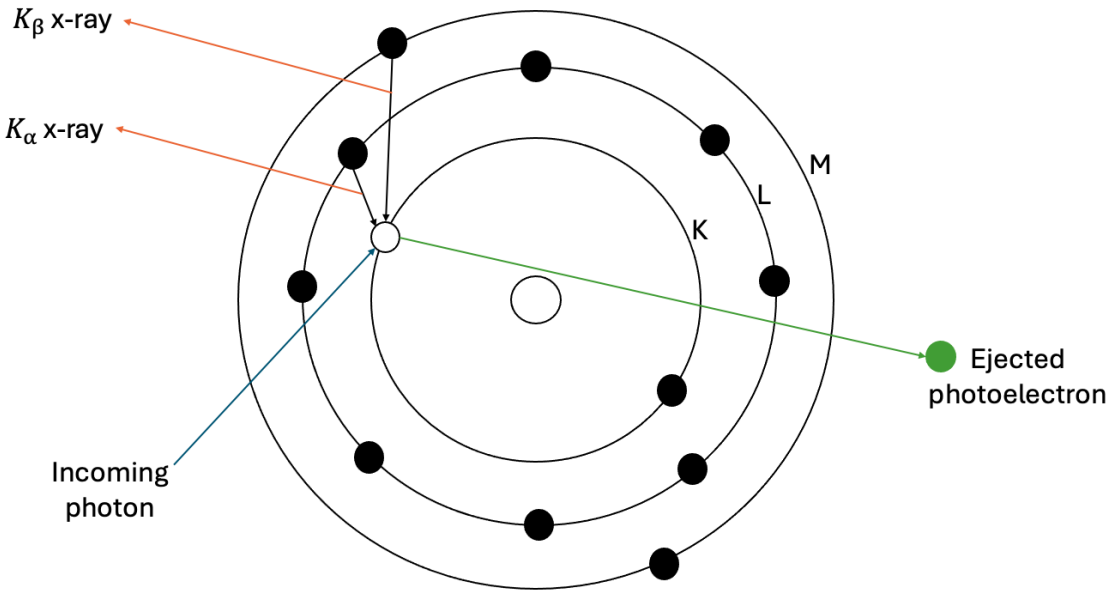

Figure 1.1: Principle of XRF. An incoming photon (blue) ejects a photoelectron (green) from the inner shell of an atom. A higher shell electron (black) transitions to fill the vacancy, emitting a characteristic x-ray (orange).

The probability of photoelectric absorption occurring is proportional to $(\frac{Z}{E})^3$, where Z is the atomic number of the target atom and E is the energy of the incident photon. Photoelectric absorption is the predominant interaction at lower energies, and increases in probability for higher Z elements. To increase the probability of photoelectric absorption happening, the K-edge of an element can be taken advantage of. The K-edge describes a phenomenon in which the probability of photoelectric absorption occurring increases greatly directly above the K-shell binding energy for an

atom. Since iron is of interest for this work, the K-edge of iron (7.1keV) can be used to encourage the likelihood of photoelectric absorption occurring. Therefore, an incident photon energy slightly above 7.1keV is optimal for promoting XRF interactions of iron.

1.4.2 Skin anatomy

The skin is part of the integumentary system, which functions to protect the body from the external environment [25]. Multiple layers make up the skin: the epidermis, dermis, and hypodermis. Iron within the epidermis varies, with most of the iron concentrated in the bottom layer, the stratum basale [26, 27]. The thickness of the epidermis varies throughout the body. Within the hand, the epidermal thickness of the palm is about 0.14 mm, and 0.09 mm on the dorsal side [28, 29].

To mimic human skin for experiments, porcine (pig) skin is often used. Pig skin is similar to human skin in structure, with the depth of the epidermal and dermal layers having similar ratios [30]. The benefit of using pig skin is that it is often readily available from butchers and does not require the same ethical approval and biosafety standards that research with human skin samples requires.

1.4.3 XRF measurements in skin

XRF has been used to measure various elements in the body including iron, copper, and zinc [31]. The non-invasive nature of XRF makes it a desirable method of carrying out in vivo measurements. Because the energy required to excite iron atoms is relatively low, the penetration depth of the incident beam is on the order of millimetres [31]. As a result, XRF measurements can be completed superficially in tissue

such as the skin.

Previous work done by researchers including Gorodetsky *et al.* and Farquharson *et al.* illustrate the ability to measure iron in the skin using an XRF system consisting of an x-ray tube [31, 32]. Participants with normal iron levels were found to have skin iron concentrations in the range of 5.6-14 ppm, while participants with iron overload had iron levels ranging from 13.7-150 ppm [31]. The skin dose participants received in this experiment was 10 mSv. Work done by Estevam and Appoloni investigated the use of a portable XRF system to measure iron in vivo [33]. While desirable due to its portablity and short measurement time of 50 seconds, this system demonstrated a minimum detection limit (MDL) of 13 ppm, which is above the expected range for normal iron levels [33]. Unfortunately, many XRF systems which use an x-ray tube result in a high MDL due to Bremsstrahlung radiation.

An ideal XRF system would be able to measure the expected range of iron, including iron deficient levels, within a reasonable measurement time. The need for a system that fulfills these requirements inspired the development of a portable XRF system which uses a radioisotope instead of an x-ray tube as the excitation source.

1.5 ^{109}Cd-based portable XRF system

As previously mentioned, XRF systems that use an x-ray tube limit the MDL of a system due to the higher amount of background radiation. Furthermore, attaining approval to use an x-ray tube for clinical purposes in Ontario, Canada is an extensive and arduous process.

This limitation can be overcome through the use of a radioisotope as the x-ray source. Radioisotopes used by other researchers to measure elements such as Fe, I,

U, and Au include ^{241}Am, ^{57}Co, ^{153}Gd, and ^{109}Cd [33]. When choosing a radioisotope for XRF, it is important to consider half-life, accessibility, and emitted energies.

The work in this thesis makes use of ^{109}Cd as the excitation source for XRF. ^{109}Cd has a half-life of 462 days, and decays by electron capture (100%) to the isomeric state of ^{109}Ag. ^{109}Ag then decays by emitting 88keV γ-rays (4%) or through internal conversion (96%). When ^{109}Ag decays by internal conversion, notable emissions are the K_α (22.1keV) and K_β (24.9keV) x-rays [34]. These x-rays are used as the excitation source for XRF.

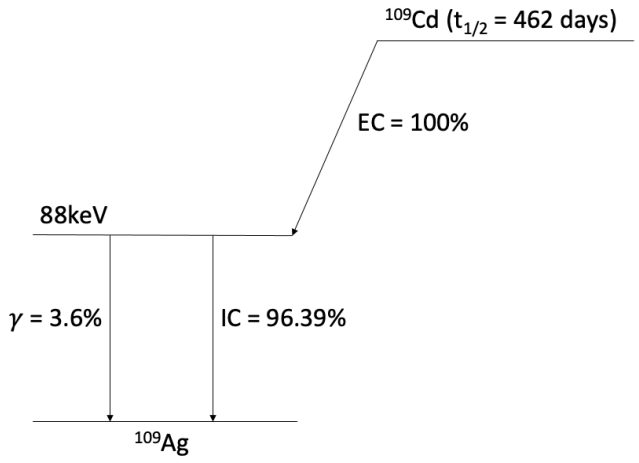

Figure 1.2: Decay scheme of ^{109}Cd.

For this work, ^{109}Cd was obtained as a sealed source from a supplier in Obninsk, Russia. The ^{109}Cd is plated on a 1mm diameter, 30μm thick silver matrix with a 100μm titanium window. The capsule that houses the source is cylindrical with diameter and height of 3mm, and is placed in a backscatter or 180° geometry relative to the silicon drift detector, as seen in Figure 1.3. The source used in this thesis was described as having an activity of 5.0GBq on 9th February 2016 by the supplier. Its

activity during this work, which began in June 2024, could be calculated as:

$$A(t) = A_0 e^{-\lambda t} \tag{1.5.1}$$

$$A = (5 \text{ GBq}) e^{-\frac{ln2}{464 \text{ days}} 3035 \text{ days}}$$

$$A = 53.7 \text{ MBq}$$

Thus, the activity of the source at the start of this work was 53.7 MBq.

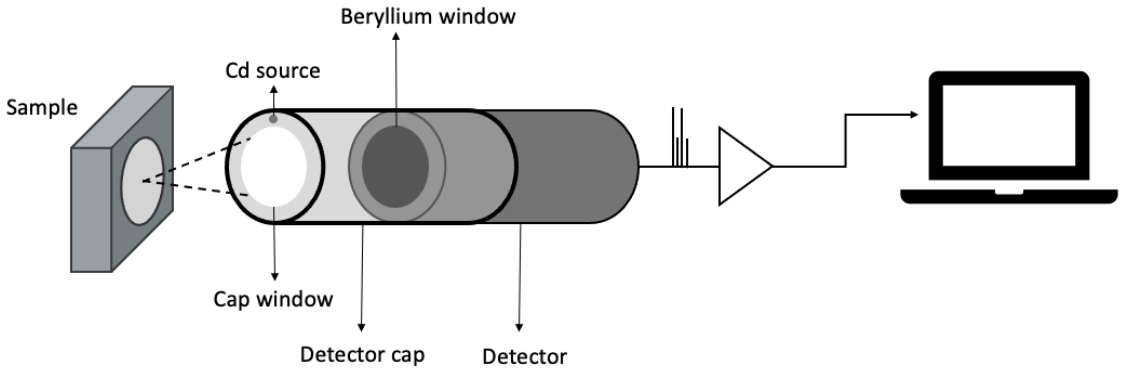

Figure 1.3: Schematic diagram of the ^{109}Cd-based XRF device used in this work.

The system is in a backscatter geometry, with the source pointing outwards parallel to the face of the detector. With the goal of moving this system into the clinical setting, the backscatter geometry aids in creating an 'all-in-one' system that can be portable as a single unit.

1.6 Project goal

The goal of this work is to determine the feasibility of using a previously developed ^{109}Cd system for in vivo XRF measurements of skin iron. While this system has demonstrated promising results for phantom and animal measurements, no in vivo applications have been investigated yet. We hope this system can be implemented as an inexpensive, non-invasive, accurate way of assessing iron levels from iron deficiency to iron overload.

Chapter 2

Methods of XRF system calibration

2.1 Chapter outline

This chapter outlines the design and setup of the XRF system for skin iron measurements. The XRF system was moved to a new laboratory and had not recently been used for measurements, thus required an improved understanding of its performance in its new location. Methods of calibration are outlined alongside an exploration of the use of hotter and colder ^{109}Cd sources.

2.2 System setup

2.2.1 Detector cap

Initially, a ^{109}Cd source of higher radioactivity, also referred to as 'hotter', was desired for this work to reduce the measurement time of the system. Increasing the activity of the source would result in more counts incident on the detector, requiring a shorter measurement time for in vivo applications. However, the hotter ^{109}Cd source obtained from the manufacturer had different specifications compared to the less radioactive 'colder' source. The hotter source had the same physical dimensions as the colder source, however suspected iron contamination was found in it through the presence of iron in collected spectra. Likely, the source encapsulation was different resulting in iron contamination. Due to the nature of this project requiring detection of low levels of iron, the iron contamination in the source needed to be filtered out.

To try to filter out the low-level iron contamination in the hotter source, a new detector cap was designed with a more collimated source holder. The goal was to ensure that the detector could 'not see' iron x-rays emitted directly from the source encapsulation. This project used a KETEK VITUS H150 x-ray silicon drift detector (SDD). The SDD has a very delicate beryllium window, which is protected by an aluminum cap. Previously, an aluminum cap with a styrene window on its circular face was used with a small tantalum source holder/collimator. The tantalum source holder had been glued externally on the face of the aluminum cap, but it was possible that the collimator was not long or thick enough to prevent iron x-rays from the source encapsulation being measured by the detector, either directly or through elastic scatterring. To try to reduce the increased iron signal from the hotter source, an

aluminum cap with lead lining was used instead. A cylindrical hole was also drilled into the cap so that the tantalum source holder could be placed flush with the face of the cap, rather than protruding from the aluminum cap. Once the source was placed inside, the front window of the cap was sealed with Ultralene XRF film (Cole-Parmer), as opposed to styrene which was used previously. XRF film is 4μm-thick film that allows high transmission of x-rays. The thin XRF film reduced attenuation of the signal compared to styrene, and ensured that the source did not fall out of the cap.

2.2.2 3D-printed phantom design

3D-printed phantoms were designed for this project using the computer aided design (CAD) software Tinkercad, visualized in Figure 2.1. The phantoms previously used for experimentation were large, having a volume of 100mL, and prone to leakage. To reduce the amount of resources used during experiments, smaller phantoms with a volume of 25mL were developed.

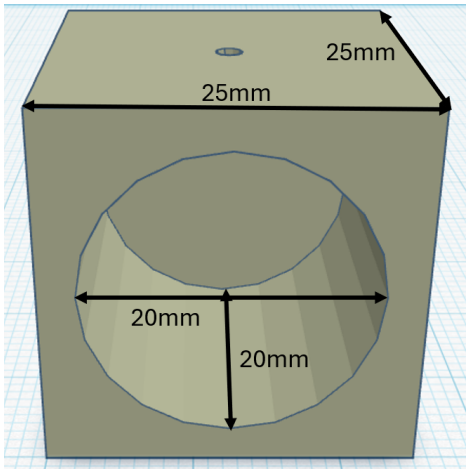

Figure 2.1: Phantom design visualized using Tinkercad software.

These phantoms were 3D-printed with an Ultimaker 2 Extended printer from polylactic acid (PLA) filament. The front circle is 20mm in diameter and sealed with XRF film using hot glue. XRF film is useful for containing liquids while maintaining transparency to x-rays to reduce attenuation for elemental analysis. This circular window allows for measurement of the liquid injected inside the phantom through the small hole (diameter = 2 mm) on the top.

An inherent challenge using 3D-printed material for holding liquids is that they are prone to leakage. Because a 3D-printer prints in layers, it is imperative that there is sufficient heat to seal the layers together; however, at boundaries where the printed shape changes, such as where the cylindrical cutout meets the posterior wall, it can be difficult for the printer to properly seal this joint. As a result, hot glue was sometimes used along the outer surface in an attempt to seal these joints to reduce leakage of the interior liquid.

2.2.3 Iron calibration solutions

The system was calibrated using iron-doped water solutions injected into the 3D-printed phantoms. For these phantoms, an iron reference standard solution of ferric nitrate ($Fe(NO_3)_3$) from LabChem were diluted using ultra-pure water to produce homogeneous calibration solutions. High purity liquid chromatography (HPLC) water (LabChem) was used for dilution to minimize potential contamination of iron in the phantoms.

Concentrations of 0, 5, 10, 15, 20, 25, 30, 50, 100, and 150 ppm were created. More solutions at lower concentrations were created as human iron levels are expected to be within this lower range; however, higher calibration concentrations were included

to improve calibration results and account for the potential use of this device in measuring patients with iron overload diseases.

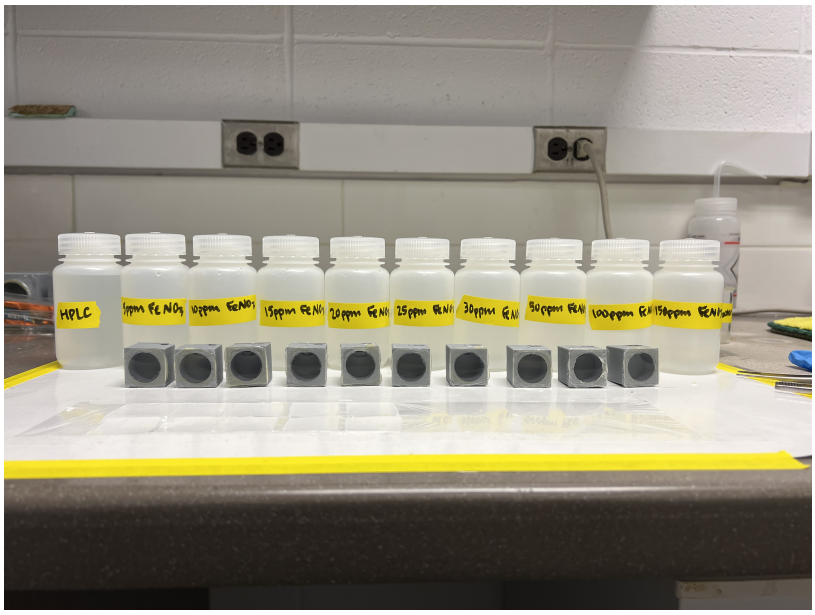

Figure 2.2: Calibration phantoms (grey) with the jars containing iron-doped water solutions behind.

The liquid phantoms were stored in 125 mL jars made from high density polyethylene with polypropylene caps (Fisherbrand) to minimize evaporation. Phantoms were filled from the solutions in these jars. A 1 mL syringe with a 20G needle attached was used to fill the phantoms through the small hole on the top. A new needle and syringe were used for each concentration to reduce the potential for improper dilution of the phantoms.

When phantoms leaked, which was inevitable due to the long-term use of them throughout this work, then they were refilled from the pre-made solutions stored in these jars. Throughout this work, the jars had to be replenished a few times for phantoms that continuously leaked, which may have led to slight variations in

the concentrations made due to inherent uncertainties in the pipette and graduated cylinder used.

2.2.4 Iron calibration analysis

After phantom calibration measurements were complete, the data was analyzed using peak fitting software. The data analysis software OriginPro from OriginLab (OriginLab Corporation) was used. The example spectra below in Figure 2.3 are visualized in the program PyMCA. The entire spectrum is shown in Figure 2.3a, with a magnification on the peaks of interest shown in Figure 2.3b.

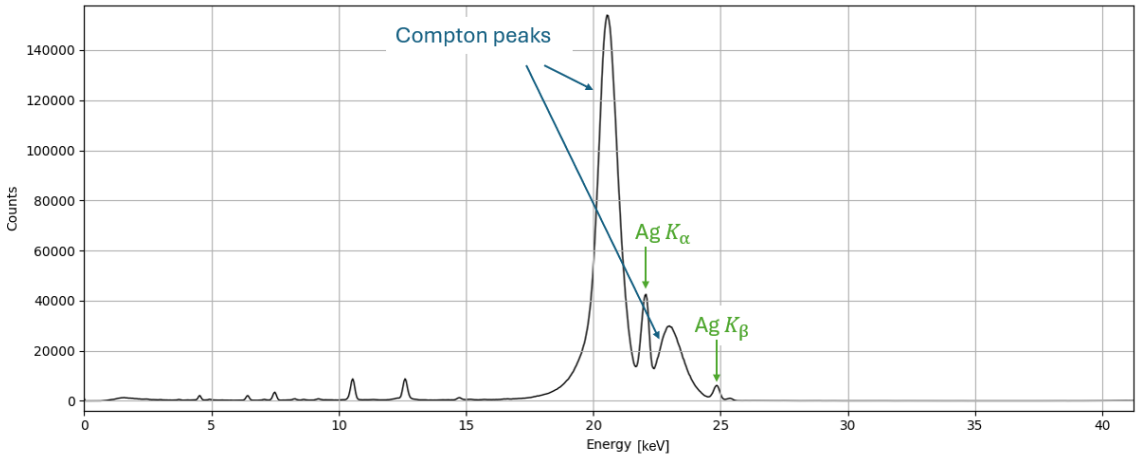

(a) The Ag x-ray peaks are labelled in green, and the Compton peaks are labelled in blue. The Compton peak per each Ag x-ray is to the left of its respective Ag x-ray peak.

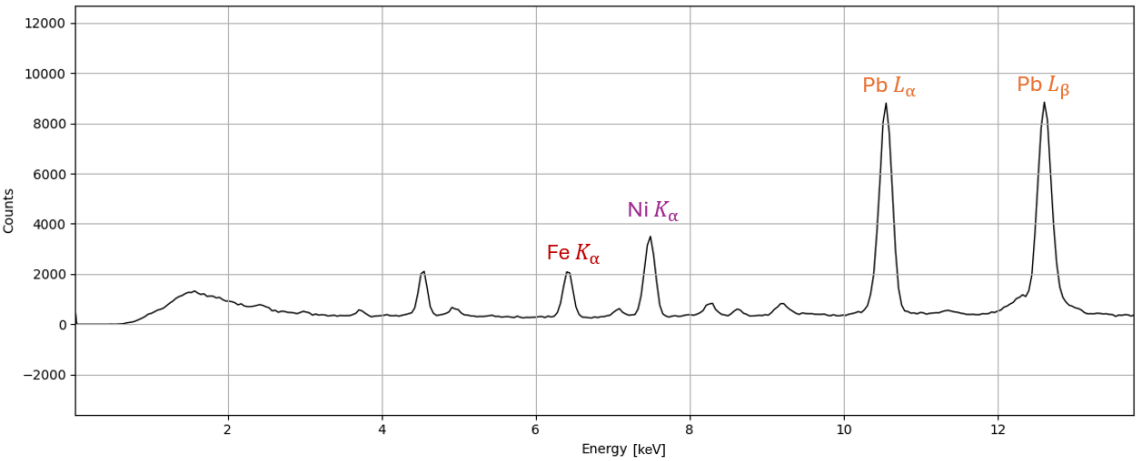

(b) Pb L-peaks are labelled in orange, and Ni and Fe K_α peaks are labelled in purple and red, respectively.

Figure 2.3: 150ppm iron phantom spectrum visualized in PyMCA.

Pb and Ni are present in the system setup, which is why they appear in the spectra. Pb is present in the detector cap, and Ni is inherently found within the detector.

A large challenge with in vivo measurements is the minute variability in sample placement relative to the detector. It is difficult for a person to keep their hand directly perpendicular to the detector at an exact distance for extended periods of time. In order to account for any effects of participant movement on the measured iron signal, the collected data had to be normalized.

As outlined in experimental work completed previous to this project, Fe counts could be normalized to another XRF peak to reduce variability due to distance from the detector [35]. Ni is present in the detector itself, and is therefore always present in the collected XRF spectra; therefore, normalization to Ni was previously performed to account for differences in sample placement, measurement time, and decay correction.

2.3 Hotter ^{109}Cd source

The initial goal of this project was to incorporate the hotter ^{109}Cd source into the XRF system. The initial calibration line created for phantom measurements with this source is below in Figure 2.4. Phantoms were measured 5 times for 1800s each.

Despite having a reasonable R^2 of 0.959, this calibration line revealed challenges with using the hotter ^{109}Cd source. In general, the calibration curve can be applied to calculate the iron concentration as follows:

$$\text{Iron concentration [ppm]} = \frac{\text{y-intercept} - \text{Normalized Fe counts}}{\text{Slope}} \tag{2.3.1}$$

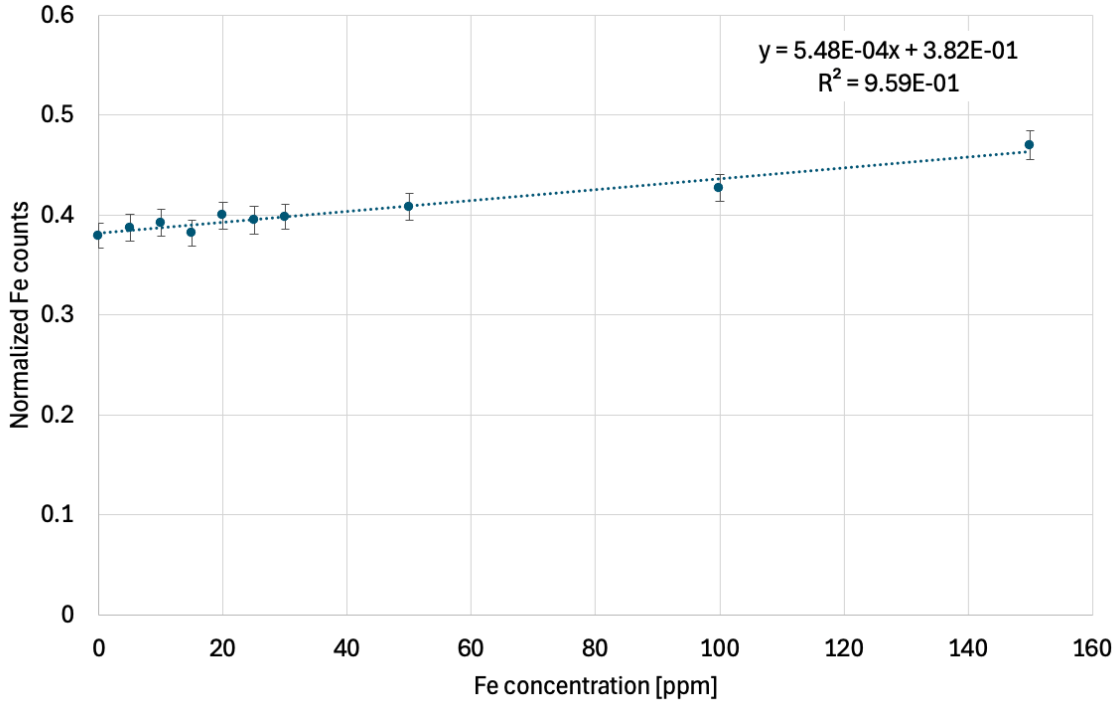

Figure 2.4: Calibration line for the hotter ^{109}Cd source. Error bars represent measurement uncertainty. The R^2 value is 0.959

$$\text{Iron concentration [ppm]} = \frac{0.000548 - \text{Normalized Fe counts}}{0.382}$$

There was a high amount of Fe signal contamination using this hotter source, as demonstrated through the high y-intercept of 0.382. This y-intercept translates to a contamination level of 697 ppm as calculated by:

$$\text{Iron contamination} = \frac{\text{y-intercept}}{\text{Slope}} \tag{2.3.2}$$

$$\text{Iron contamination} = \frac{0.382}{0.000548}$$

$$\text{Iron contamination} = 697 \text{ ppm}$$

This demonstrates that even when measuring a 0ppm Fe phantom, there was a very high Fe signal present in the detector setup that made it difficult to measure trace amounts of iron. This suggested inherent contamination, probably from the source encapsulation, that is unavoidable using this detector system.

2.3.1 Pig skin measurements

The feasibility of using the hotter ^{109}Cd source was determined after measuring a sample of pig skin with this setup. A pig skin sample was obtained from a local butcher in Dundas and cut to fit the previously designed 3D-printed phantom. The sample was measured in a 3x3 grid style to investigate the heterogeneity of iron distribution throughout pig skin.

Orientation of pig skin	Left	Middle	Right
Top	41	-32	-45
Middle	25	-13	-50
Bottom	27	-11	-12

Table 2.1: Iron concentration [ppm] in pig skin as calculated using the calibration line from the hotter ^{109}Cd source in Figure 2.4.

Viewing the values in Table 2.1, it can be seen that the high iron contamination from the hotter source makes it extremely challenging to measure trace amounts of iron in the skin, which was previously performed by Bangash *et al.* using the colder ^{109}Cd source [36]. The values in Table 2.1 did not align with expected iron levels in pig skin, which ranged from 7.7-14 ppm in the other study [36].

Furthermore, the hotter ^{109}Cd source was purchased with the intention of it being 10x hotter, in other words with 10x the number of ^{109}Cd Ag x-ray emissions. However, the relative increase in Ag x-rays does not correlate with the increased source activity.

Measurements taken by Bickley *et al.* of the two ^{109}Cd sources through a pinhole collimator with a hyper-pure germanium (HPGe) detector showed that the Ag x-rays were decreased in the hotter ^{109}Cd source relative to the 88 keV γ-ray from electron capture, as seen in Figure 2.5 [37].

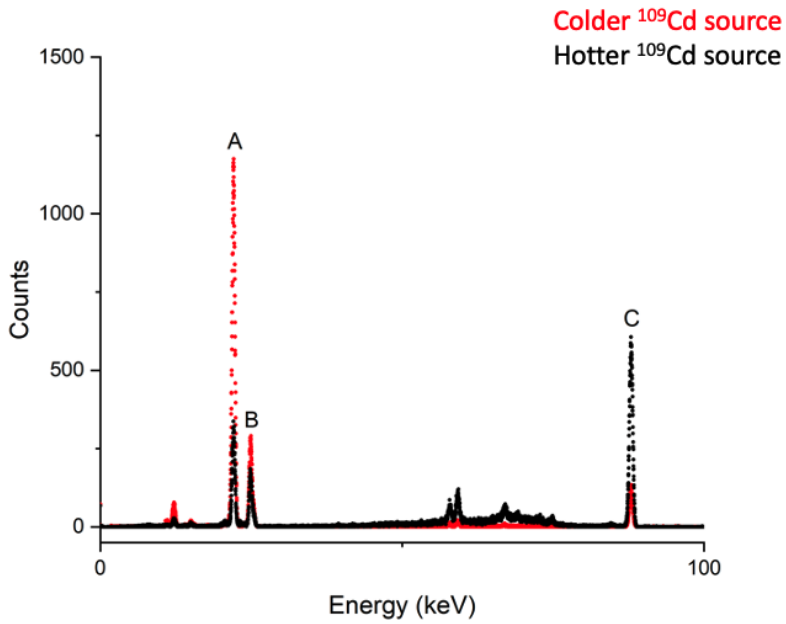

Figure 2.5: Comparison of the hotter ^{109}Cd source (black line) versus colder ^{109}Cd source (red line). Peaks A and B are the Ag x-rays at 22.1 and 24.9 keV, respectively. Peak C is the 88 keV γ-ray from electron capture [37].

Bickley *et al.* performed a crude estimate that suggested there is 200 μm of additional steel in the encapsulation of the hotter ^{109}Cd source from this data [37]. This further supports the previously discussed iron signal contamination that is observed from the hotter ^{109}Cd source. The hotter ^{109}Cd source thus was found to have more emissions of higher energy γ-rays, contributing further to dose with little contribution to signal, without a similar increase the relevant Ag x-rays required for XRF purposes.

2.3.2 Minimum detection limit

The minimum detection limit (MDL) of the system as previously calculated was 1.35 ppm [35]. This was possible for measurement times of 1800 s; however, the goal of this work is to reduce the measurement time to make in vivo measurements feasible and more practical. Furthermore, the ^{109}Cd source had decayed since these calculations were performed. The loss in activity worsens the MDL since there will be fewer counts incident on the sample and thereby the detector.

As has been the conventional method in our laboratory for several decades, the MDL can be calculated from the uncertainty in the 0 ppm phantom measurement as:

$$\text{MDL} = \frac{2 \times \sigma_{0 \text{ ppm}}}{\text{Calibration slope}} \tag{2.3.3}$$

The MDL of the system with the hotter ^{109}Cd source (Figure 2.4) was calculated as:

$$\text{MDL} = \frac{2 \times 0.012}{0.00548}$$

$$\text{MDL} = 43.8 \text{ ppm}$$

An MDL of 43.8 ppm is far higher than the previous MDL of 1.35 ppm, and would not be sufficient to measure low to normal in vivo levels of iron. While it might still be possible to measure high levels of iron with this MDL, this would not be reasonable for clinical applications.

As a result of the small increase in Ag x-rays, iron signal contamination, and the high MDL, it was decided that the small advantage conferred by using a hotter source was not worth the challenges brought forth from the suspected different encapsulation

of the hotter the source. Therefore, a decision was made to move forward with using the previous colder ^{109}Cd source for in vivo measurements.

2.4 Colder ^{109}Cd source

After the system source was swapped from the hotter to colder ^{109}Cd source, a new calibration line had to be created.

Each phantom was measured for 1200 s at least 5 times in a random order. Previous experiments with this device measured phantoms for 1800 s, however, this is a long time for in vivo measurements. 1200 s was chosen for measurements to decrease measurement time but still collect sufficient data to minimize uncertainties. Repeat measurements were valuable for refining the calibration measurements, as well as understanding the reproducibility.

Preliminary Fe calibration counts were normalized to Ni counts, and the corresponding errors were summed in quadrature. To determine measurement reproducibility, a 15 ppm Fe phantom was measured for 1200 s multiple times over different days. The phantom was removed and replaced after each measurement to observe how positioning and normalization might affect the measurement results. The results of these data are illustrated below in Figure 2.6.

The large variation with lack of overlap in error bars illustrated in Figure 2.6 suggested that normalization to Ni was not sufficient to account for measurement uncertainties. While Ni normalization may have corrected for distance differences in previous work, it was not sufficient for the new setup of the XRF system.

To account for these differences, normalization to an alternative peak in the spectrum was investigated. It was found that normalization to the Compton peak of the

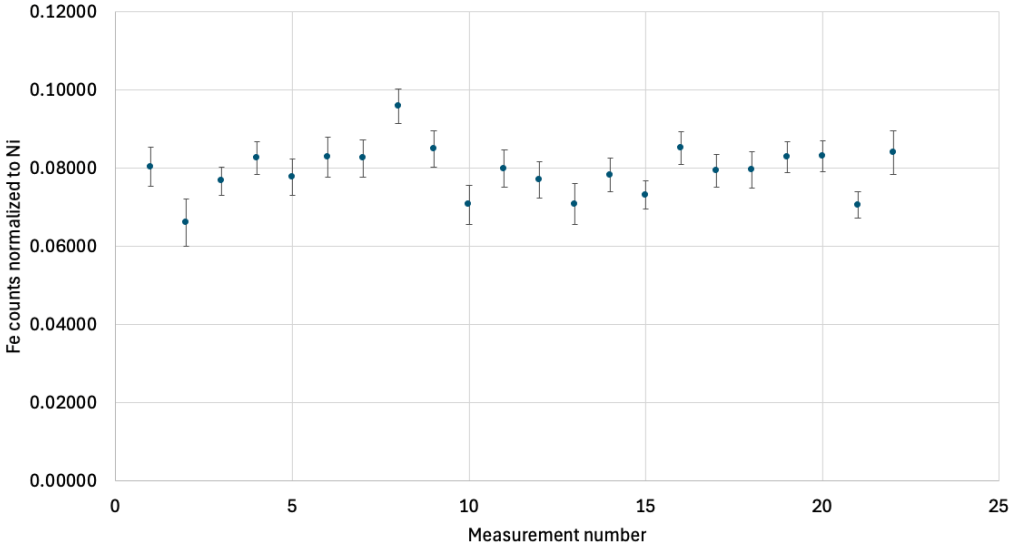

Figure 2.6: Repeat measurements of a 15 ppm Fe phantom, with Fe counts normalized to Ni counts. Error bars represent measurement uncertainty. Measurements were 1200 seconds.

22.1 keV Ag x-ray conferred slightly better results, seen in Figure 2.7. The Compton peak has greater counts and thereby lower uncertainty from Poisson counting statistics. Therefore, this normalization was used for the remainder of the data analysis in this work.

To determine what other uncertainties may be affecting the system, repeat measurements of a 100 ppm Fe phantom were carried out without moving the phantom. As mentioned previously, these phantoms were prone to leakage and had to be moved once during this process to clean up the leaked liquid before further measurements were carried out. The variation in counts are visualized in Figure 2.8.

It can be seen that there is still a large variation in measurement results, even without moving the phantom between measurements. Because of this, it is thought

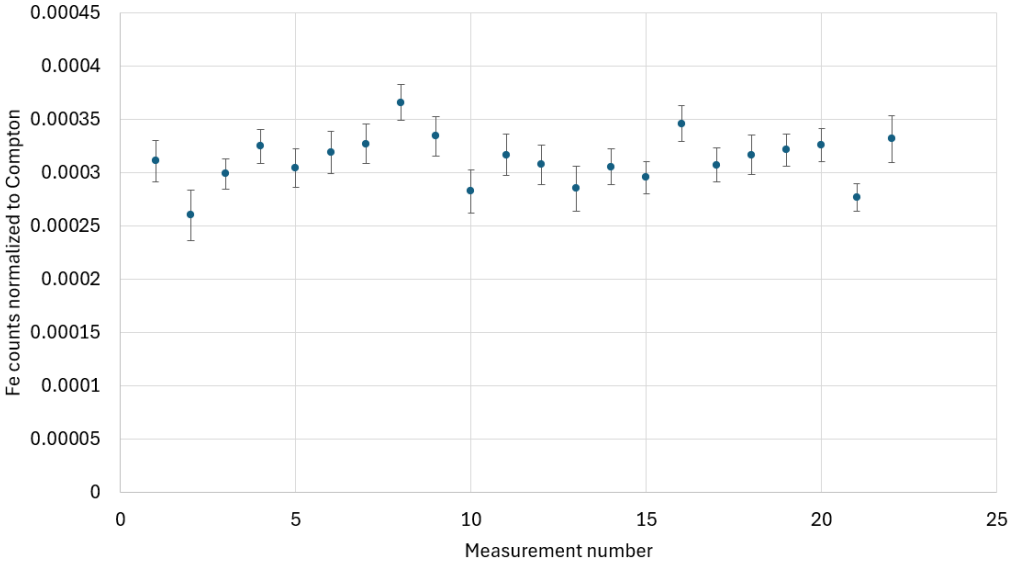

Figure 2.7: Repeat measurements of a 15 ppm Fe phantom, with Fe counts normalized to Compton counts. Error bars represent measurement uncertainty. Measurements were 1200 seconds.

that the inherent counting uncertainty from Poisson statistics was leading to these results. Moving forward, longer counts were performed to reduce relative measurement uncertainties from Poisson variations due to radiation measurement versus potential factors such as sample placement or orientation.

2.5 Conclusion

The work in this Chapter demonstrated that while a hotter ^{109}Cd source was initially intended for this project, this was not feasible based on the presented findings. Lack of benefits conferred from this hotter ^{109}Cd source resulted in moving forward with the colder ^{109}Cd source instead. While normalization to Ni counts was previously used, this was not as suitable for the new setup therefore normalization to the Compton

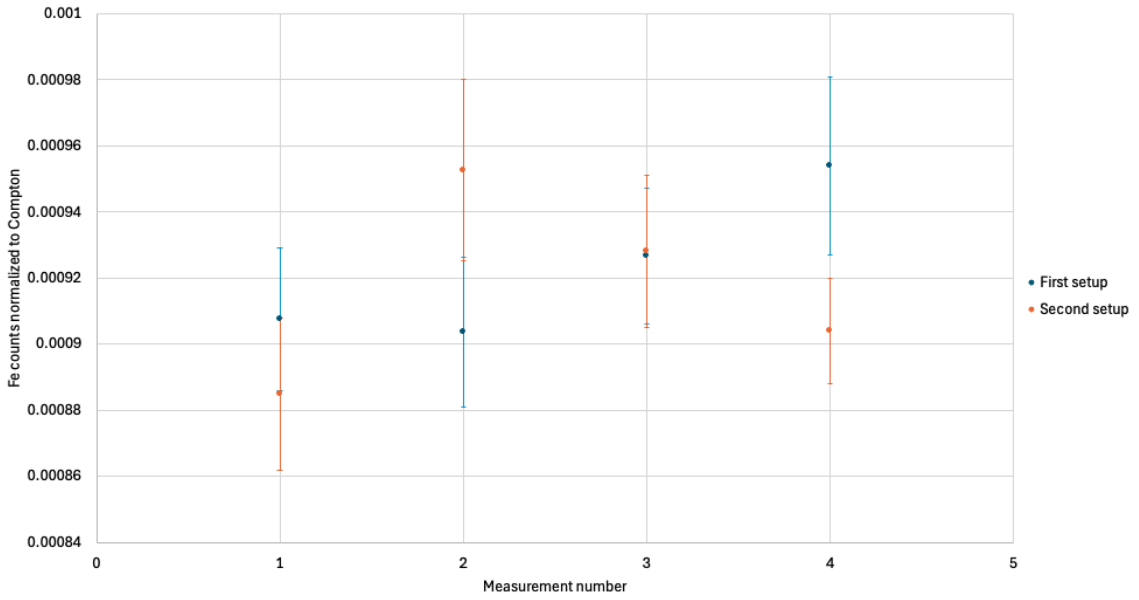

Figure 2.8: Repeat measurements of a 100 ppm Fe phantom, with Fe counts normalized to Compton counts. Error bars represent measurement uncertainty. Measurements were 1200 s, and the phantom was not moved except for between data sets 'First setup' and 'Second setup' due to phantom leakage.

peak was implemented for future analysis.

2.6 Chapter summary

In this Chapter, calibration methods and preliminary system optimizations for the ^{109}Cd-XRF device were explored. Changes were made to the detector cap to make it more suitable for eventual in vivo measurements. A different detector cap with a lead lining was tested with the goal of reducing iron signal contamination from the hotter ^{109}Cd source. Furthermore, a small hole was drilled in the cap to fit the tantalum ^{109}Cd source holder and ^{109}Cd source so it was flush with the detector cap. The styrene previously placed over the detector cap was replaced with XRF film to

decrease signal attenuation.

Calibration solutions were made from iron-doped water phantoms. A ferric nitrate solution was diluted with HPLC water in 10 concentrations of 0 to 150 ppm, with most of the concentrations at the lower range to mimic expected human concentrations for normal iron levels. These solutions were injected into 3D-printed phantoms sealed with XRF film for measurement.

While a hotter ^{109}Cd source was desired for further work on this project, the inherent iron contamination in the manufacturing of the source prevents its use for this work to measure trace amounts of iron. Negative calculations of iron concentration in a pig skin sample reinforced the challenges using this source would pose. Additionally, the different manufacturing of the hotter ^{109}Cd source results in attenuation of the relevant Ag x-rays and a reduced emission rate. Therefore, the hotter ^{109}Cd source was replaced with the previously used colder ^{109}Cd source. The colder ^{109}Cd source was used for the remainder of the work in this thesis.

Finally, normalization to the Compton peak was found to be more suitable for the present XRF setup compared to the previously used Ni normalization.

Chapter 3

Methods of system design

3.1 Chapter outline

In this chapter, developments towards the in vivo measurement system are discussed. An optimization of the system was required to discern the best setup in terms of sample distance and orientation towards the source and detector. For in vivo measurements, a device that could restrain the hand during measurements needed to be designed. Other findings regarding the implementation of the hand holder are investigated and discussed.

3.2 Measurement distance and orientation

The distance between the detector and the sample affects incident flux as well as irradiated area. To determine the area irradiated, x-ray chromatography film was placed at different distances from the source, and the diameter of the darkened area was measured. At 0.5 cm distance, the spot size irradiated was about 0.5 cm in

diameter, shown in Figure 3.1.

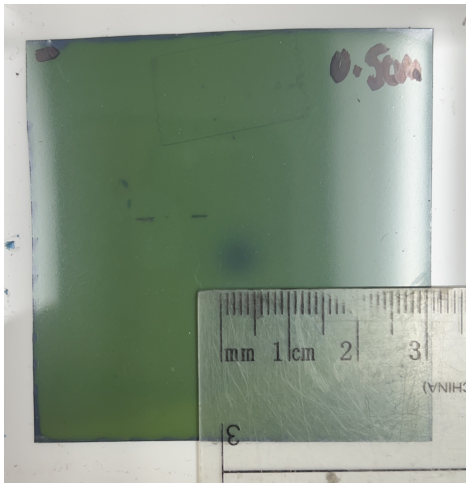

Figure 3.1: Radiochromic film demonstrating irradiation area 0.5 cm distance from the source.

To determine what spot size/distance was optimal for measurements, especially considering the decay in activity since the system was last used, an optimization comparison between various orientations towards the detector was carried out. A 150 ppm Fe phantom was measured for 600 s at different distances (0.5 cm, 1 cm) and vertical placements (centred on the source or the detector). The results are outlined in Table 3.1:

Sample-detector distance:	1cm		0.5cm	
Sample centred on:	Source	Detector	Source	Detector
Normalized Fe counts	0.513 ±0.01	0.539 ±0.01	0.459 ±0.008	0.491 ±0.01

Table 3.1: Normalized Fe counts at different sample orientations relative to the detector.

As most of this work focuses on the uncertainty in measurements, this was taken into consideration to determine which orientation was best for remaining measurements. The uncertainty was lowest for the orientation in which the sample was centred

on the source at 0.5cm distance, therefore measurements were performed using this setup.

Note that this varies slightly from the area measured for dosimetry purposes by Bangash *et al.*, in which the dose to 0.8 cm^2 of skin was 1.1mSv in 2021 [35]. Due to decay of the source since this measurement, the dose to the skin would be less due to decreased count rate, and therefore still suitable for human measurements.

3.3 Handholder design

The XRF device is setup on top of an optical table, which has holes every 2.5cm into which items can be secured with screws. This allows all aspects of the system to be secured to minimize movement during the measurement. In alignment with previous requests from Health Physics at McMaster University, an acrylic sheet was placed on top of the optical table to minimize the chance for small radioactive sources to be lost in the holes of the table. To access the holes to screw down items, the acrylic sheet was drilled through to access specific holes.

The detector was mounted to a small scissor lift that can be raised and lowered. This lift can be moved allowing for precise placement. It is secured on either side with small metal plates screwed into the table, shown in Figure 3.2.

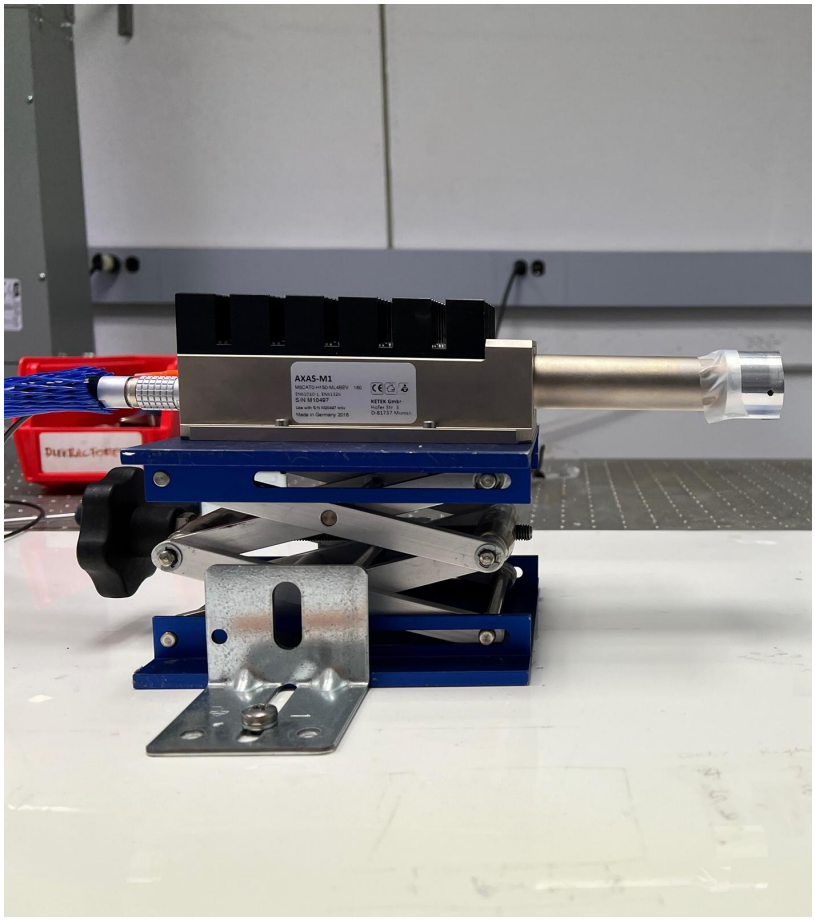

Figure 3.2: SDD mounted on a blue scissor lift. The lift is secured in place using metal plates on either side that are screwed into the optical table below an acrylic sheet.

The hand holder was designed as a main block with a hole for the detector and an area for the hand to rest, with a back block that would hold the hand in place. The device is visualized in the CAD program Tinkercad in Figure 3.3. This setup would allow the hand to be secured in place to minimize movement during in vivo measurements, while still allowing for flexibility to accommodate different hands. This meant that the holder and detector could accommodate different hand sizes by thickness, through the movement of the back block, and width, through vertical adjustment of the detector through the rectangular window.

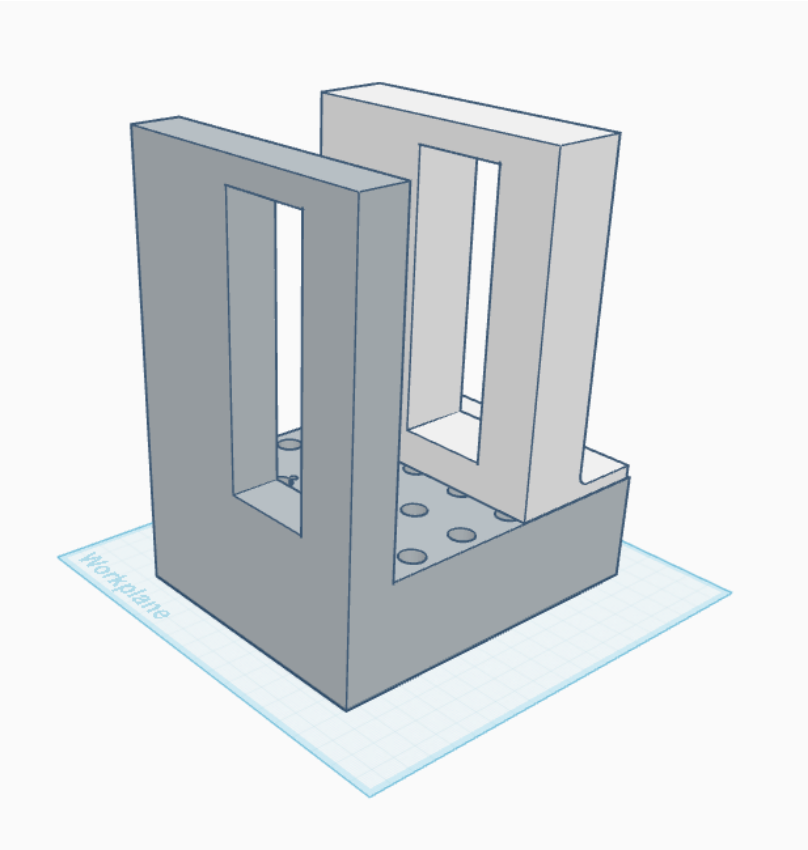

Figure 3.3: Hand holder device visualized in Tinkercad. The main block is in dark gray and the back block is in light gray.

The main block has holes that align with the holes in the optical table so it can

be secured. The back block needed to be adjustable so that it could accommodate various hand thicknesses. The back block is secured to the optical table with a metal plate that presses down on the small lip at the back of the block. The back block has a window identical to the main block to minimize potential backscatter. Figure 3.4 shows the 3D-printed hand holder mounted on the acrylic sheet with the detector placed appropriately.

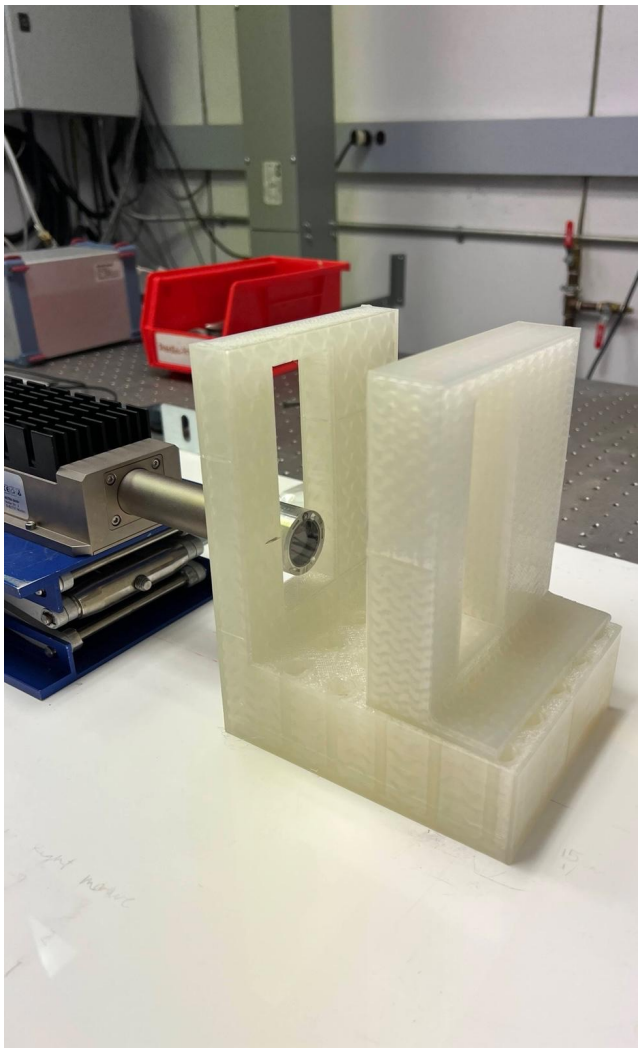

Figure 3.4: The 3D-printed hand holder mounted on top of the acrylic sheet. The detector is placed through the window of the main block.

The filament chosen for printing the hand holder was a natural PLA with no added colouring (Matter3D). This was done to minimize the potential for trace iron to be introduced into the material during the manufacturing process. The specific filament used was described by the manufacturer as being derived from pure virgin PLA pellets. Although this device would not be measured directly, it was important to reduce iron contamination in the surrounding environment, which could be excited from scattered photons. The hand holder was printed using an Ender-3 V2 3D-printer with 20% infill, as one roll of filament would not have been sufficient to print at 100% infill.

3.4 Horizontal placement within the hand holder

While carrying out calibration measurements after implementing the hand holder, differences in measurement results were discovered. As shown in Figure 3.5, there was a difference in measurement results, where the presence of the hand holder resulted in higher normalized Fe counts. The difference in the two slopes is statistically significant ($p < 0.0002$), suggesting a greater signal.

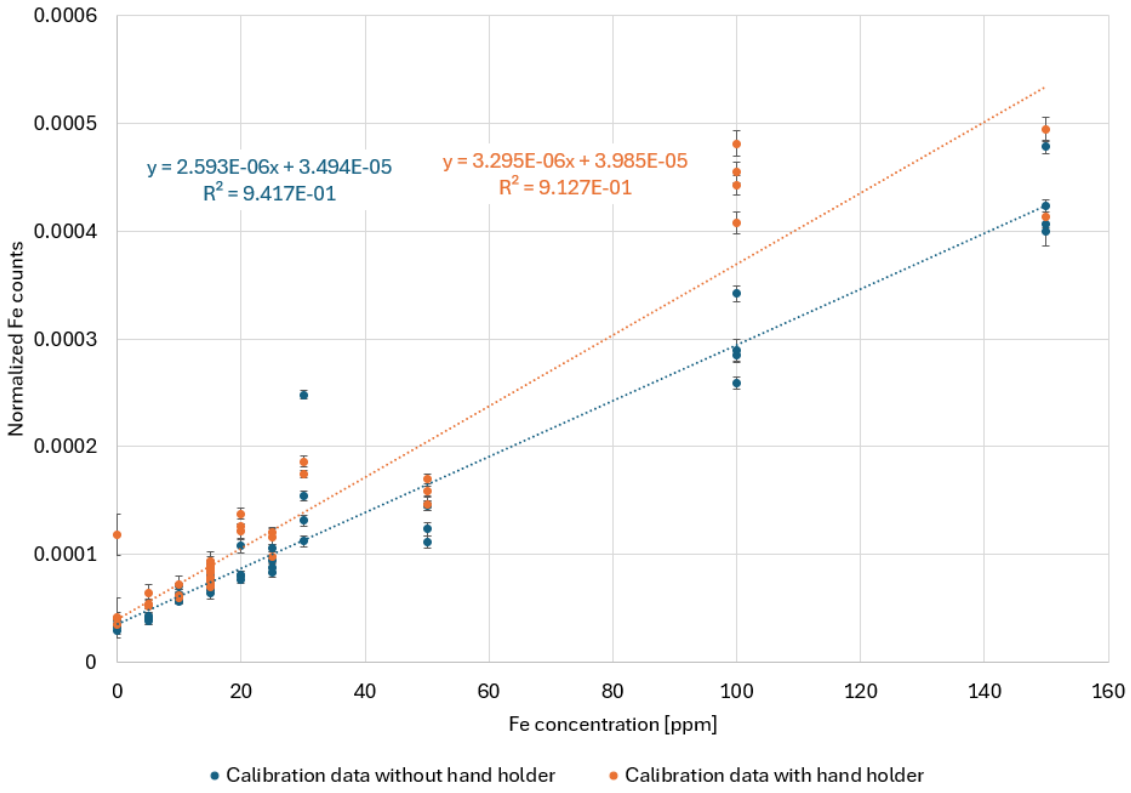

Figure 3.5: Comparison of calibration phantom measurements done without the hand holder (blue) versus with the hand holder implemented (orange). Fe counts are normalized to the Compton peak. Error bars represent measurement uncertainty.

To better understand the influence of the hand holder on measurements, an investigation into horizontal placements within the hand holder was carried out. A 150 ppm Fe phantom was placed at different distances into the hand holder (0, 0.5, 1, and 1.5 cm) to mimic how hand tissue can enter into the window of the hand holder when the hand is secured.

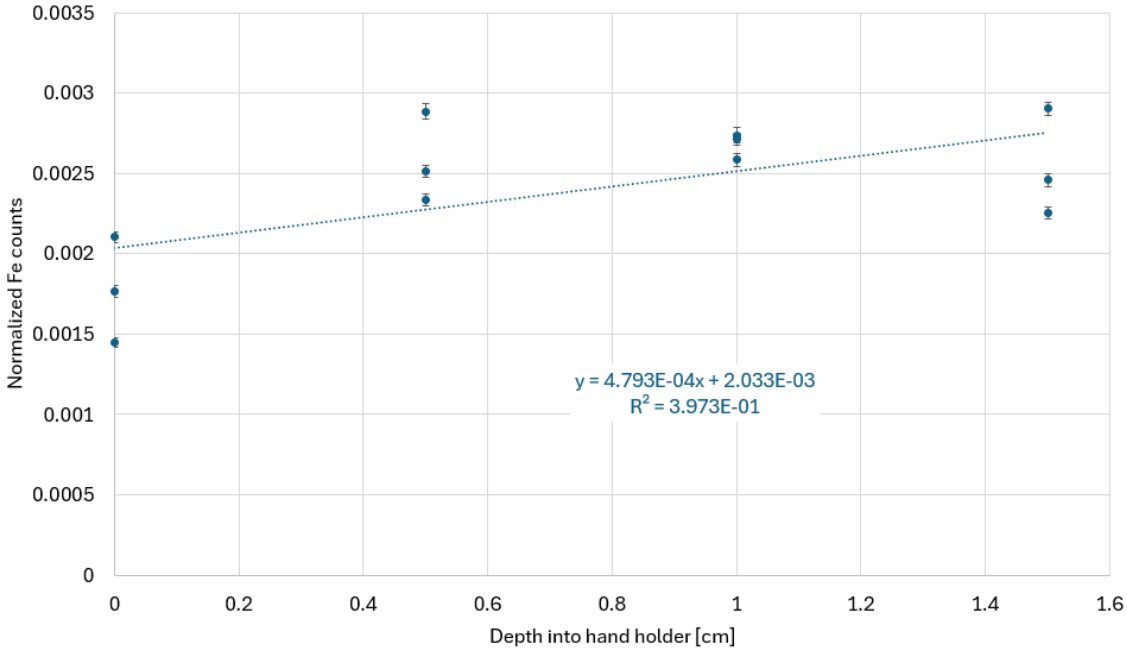

Figure 3.6: Normalized Fe counts versus phantom placement at different depths into the hand holder. Fe counts are normalized to Compton counts. Error bars represent measurement uncertainty. The R^2 value is 0.40.

Examining Figure 3.6, it can be seen that there is some slight variation as the sample extends further into the hand holder. Notably, there is a difference in normalized Fe counts when the detector is in the holder. Although the R^2 of 0.40 suggests only a moderate correlation, this can be largely influential for a calibration line. The drastic effect can be visualized in Figure 3.7 below.

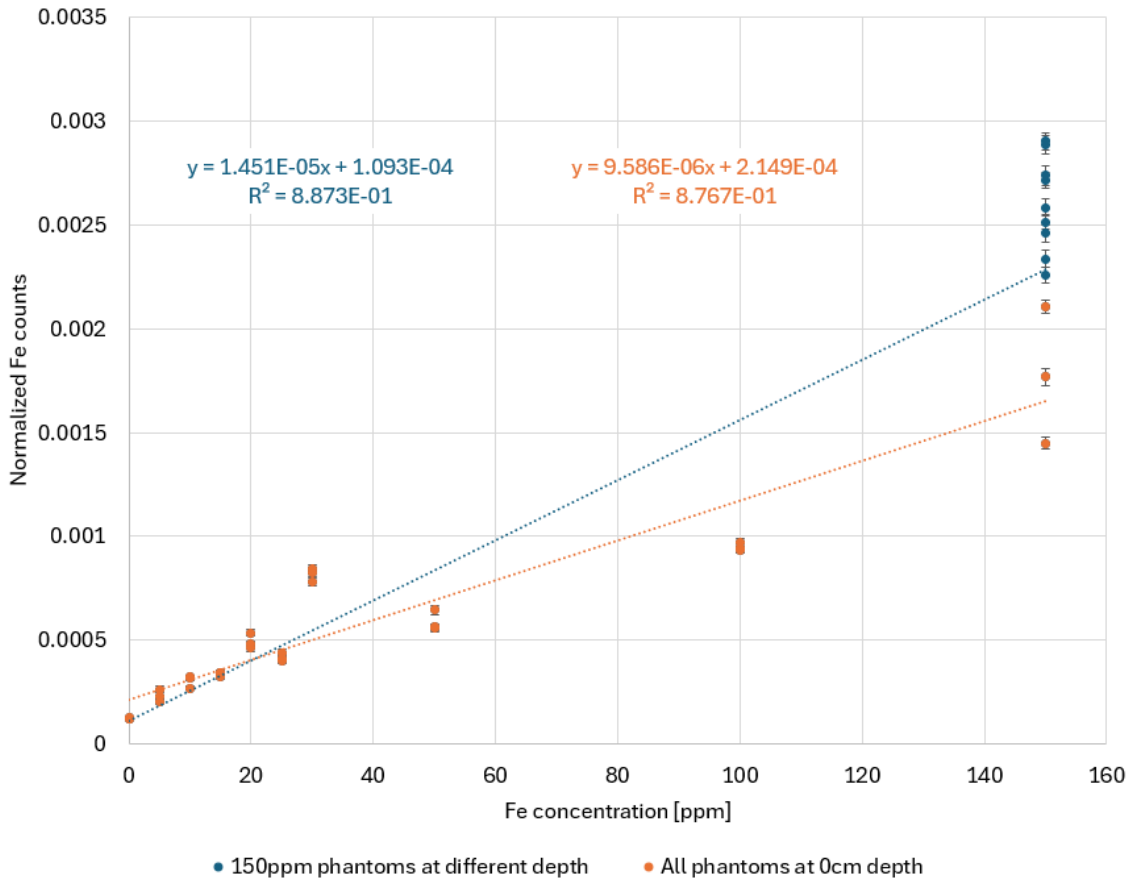

Figure 3.7: Comparison of calibration phantom measurements with phantoms at different depths within the hand holder. The blue calibration line plots all phantom data, including those in which the 150 ppm phantom was placed at different depths into the hand holder. The orange data plots only phantom measurements during which the phantoms were placed at 0 cm depth, in other words not within the hand holder. Fe counts are normalized to Compton counts. Error bars represent measurement uncertainty.

It can be seen that inclusion of measurements at various depths into the hand holder greatly affects the calibration line ($p < 0.0001$). As a result, this should be taken into consideration when measuring phantoms. An alternate method of accounting for these placement differences should be considered, as consistency in sample placement can be challenging during in vivo measurements.

Another concern that needs to be addressed is the large variability in the data shown in Figure 3.7. While some Fe phantoms produced consistent measurements (e.g. 100 ppm), others do not (e.g. 150 ppm). Additionally, some Fe phantoms (e.g. 20 ppm, 30 ppm) were consistently higher in iron than expected relative to the eight other phantoms. In order to obtain a calibration line that could reliably predict iron concentration, new phantoms were printed and measured, as discussed in the following section.

3.5 Calibration line

In order to minimize error from counting statistics and reduce measurement variability, longer measurement times were desired to produce the calibration line. However, as mentioned previously, the phantoms were prone to leaking. This is possibly in part due to the printing parameters, but also could be due to prolonged use of the phantoms. As a result, new phantoms were created to see if the old phantoms were contributing to the wide variability that was observed. The new phantoms were of the same design as the previous phantoms, but printed from the colourless PLA of which the hand holder was made.

Phantoms were remeasured for count times that resulted in excess of 10,000 counts being collected for the Fe peak. This was done to ensure that the relative uncertainty

in the measurement from counting statistics was less than 1% due to Poisson statistics, from relative uncertainty = $\sqrt{N}/N$. Because a ratio is taken to normalize the Fe counts, the count time could be varied between phantoms. Phantoms were measured at least three times and the data for the Fe counts normalized to the Compton peak of the 22.1 keV Ag x-ray are plotted for the calibration line below in Figure 3.8. In comparison to previous phantom measurements, these phantoms were not refilled throughout these longer counts which minimizes variability in the phantom concentrations over repeat measurements.

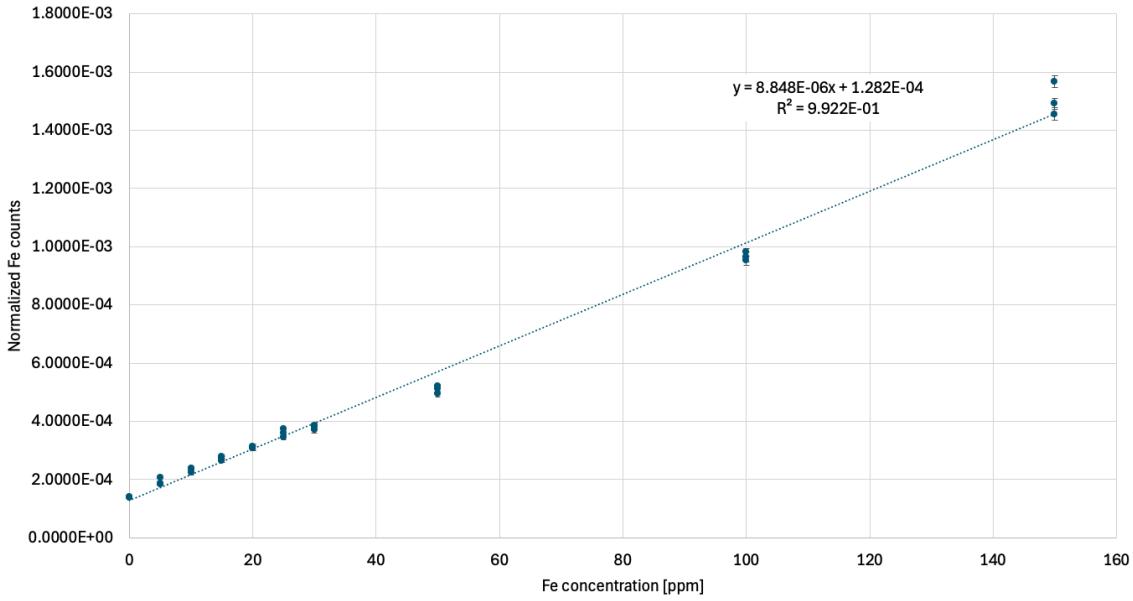

Figure 3.8: Calibration line with Fe counts normalized to Compton counts. Error bars represent measurement uncertainty. The R^2 value is 0.992.

The reduction in relative uncertainty results in a calibration line with $R^2 > 0.99$. This new calibration curve estimates an iron signal contamination level of 14.5 ppm, as calculated according to Equation 2.3.2. The MDL of the system is calculated as 2.5 ppm by Equation 2.3.3. This MDL is worse than previously attained with this

system due to source decay and shorter measurement time, however it is still sufficient to measure the lower range of expected iron levels in humans by these results.

3.6 Conclusion

The findings in this Chapter uncovered the challenges brought forth from the hand holder that was designed for future in vivo measurements. While the hand holder is required for human measurements, it altered the collected spectra, likely due to scatter. For accurate calibration results, representative measurements needed to be done of phantoms with the hand holder in place for long measurement times.

3.7 Chapter summary

In this Chapter, further optimization and development of the XRF system for in vivo measurements were discussed. Investigation into the optimal measurement distance and orientation discovered that a sample-detector distance of 0.5 cm centred on the source minimized measurement uncertainty; therefore, this setup was used for future measurements.

A hand-restraining device was developed and 3D-printed for eventual in vivo use. This device was printed from colourless PLA, and is made up of two major parts: the main block and the back block. The main block has a window for the detector, and the back block has an identical window to minimize scatter. These pieces are fixed in place with metal plates and screws that anchor into the optical table on which the XRF system is setup.

Throughout calibration measurements, it was found that the presence of the hand

holder influenced the measurements, likely through increased scatter. An investigation into the effects of the hand holder demonstrated that samples placed within the holder result in higher levels of iron. As a result, it is important to take this into consideration for future design iterations of the hand holder system, or novel methods of data analysis should be explored that can account for these placement differences.

Lastly, a new calibration line was created for the system with newly printed phantoms. Large variations in the measured phantoms prompted the printing of new phantoms due to potential contamination from prolonged use. Furthermore, phantoms began leaking so they needed to be remade in order to measure them for sufficient time to collect an excess of 10,000 counts. Both of these methodology changes resulted in a more reliable calibration line that could be used moving forward.

Chapter 4

Methods of in vivo measurements

4.1 Chapter outline

In this chapter, the experimental methodology and results of an in vivo iron study are discussed. Details regarding recruitment and study population are outlined, and iron measurement results are calculated based on the previous calibration line. Analysis of measurement uncertainties examine the feasibility of in vivo measurements moving forward. Future work and improvements are also explored.

4.2 In vivo measurement site

For in vivo measurements, the thenar eminence of the hand was chosen as the measurement site. This site was chosen for a multitude of reasons: proximity to bony features, ease of access, and radiation dose.

The thenar eminence is located on the palm of the hand at the base of the thumb. It is easy to locate on hands of different sizes due to the bony features of the phalanges,

therefore it is a reproducible measurement site. Furthermore, the hand is a fairly accessible measurement site as gloves can be removed or sleeves can be rolled up during measurements. Lastly, the radiation dose delivered to the thenar eminence is less significant due to its position as an extremity that is distal to the torso, where many critical organs are located.

Previous work by Gorodetsky *et al.* measured the thenar eminence as one of the skin sites for Fe and Zn measurements [31]. Furthermore, Dao demonstrated a correlation between skin iron at the thenar eminence and liver iron from cadaver measurement [38]. Given this previous work, the thenar eminence was a suitable choice for skin iron measurements that can predict iron levels in an organ at risk, the liver.

4.3 Ethics application and experiment design

This work involves human participants, therefore the research study needed to be approved by an ethics board. This work was submitted to and approved by the Hamilton Integrated Research Ethics Board (HiREB) for approval (Study ID #16926). Because of the use of human participants, the ^{109}Cd source license also needed to be amended by the Canadian Nuclear Safety Commission (CNSC).

For this study, 24 healthy participants (i.e. with no known iron diseases) were recruited through posters and emails to specific departments at McMaster University. This number of participants was measured in order to collect sufficient data to compare in vivo data to phantoms and ex vivo pig skin studies. Data on age and gender were collected at the time of measurement by the student researcher to discern potential performance-related issues attributed to factors such as motion, age, or gender.

Participants within the age range of 18-76 were recruited, and an equal number of male and female participants (12 male and 12 female) were measured. Volunteers who had previously taken iron supplements but were not using them at the time of measurement were permitted to participate in the study. However, participants who were taking iron supplements at the time of measurement were excluded from measurement.

Measurements took place at McMaster University's Main Campus, in the General Sciences Building (GSB). Participants met with the student researcher after email correspondence confirming interest and qualification for this study. In the lab, participants were given a copy of the study protocol and consent form to read. They were given the opportunity to discuss any questions or concerns with the student researcher. After consent was collected, the participant was brought into the study room where they were instructed to place their hand in a specific orientation relative to the detector system, as visualized in Figure 4.1. The hand was secured in place to reduce motion during the 1200 s measurement.

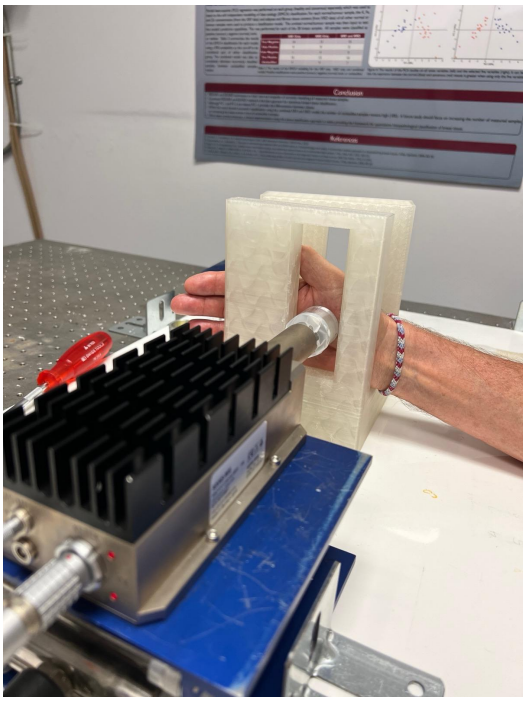

(a) Front view of the hand holder system.

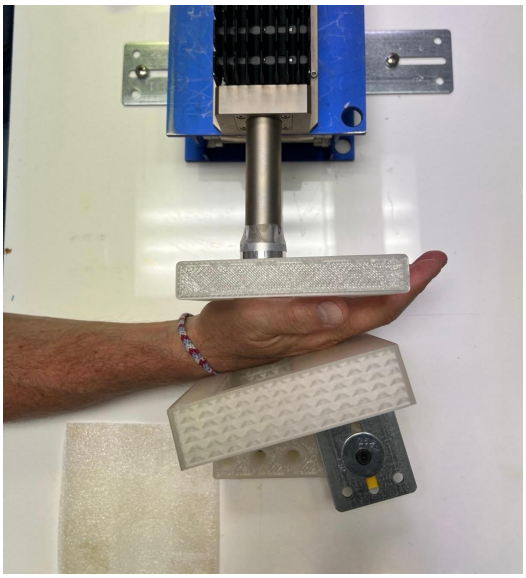

(b) Top view of the hand holder system.

Figure 4.1: Example of the setup for the XRF system for in vivo measurements (Participant 023).

While participants were being measured, a short questionnaire was delivered asking for information regarding age and gender, which was recorded strictly according to the study's HiREB approval so that this information would remain confidential. Data on gender rather than sex was collected to observe if gendered behaviours may affect skin on the hand, potentially affecting measurement precision.

During the 1200 s measurement time, participants were free to converse with the researcher, use their phone, or remain in silence. After the 1200 s measurement time, the participant's hand was released from the holder and they were free to leave.

4.4 Results

An example spectrum (Participant 024) is displayed below in Figure 4.2, focused on the relevant area of the spectrum.

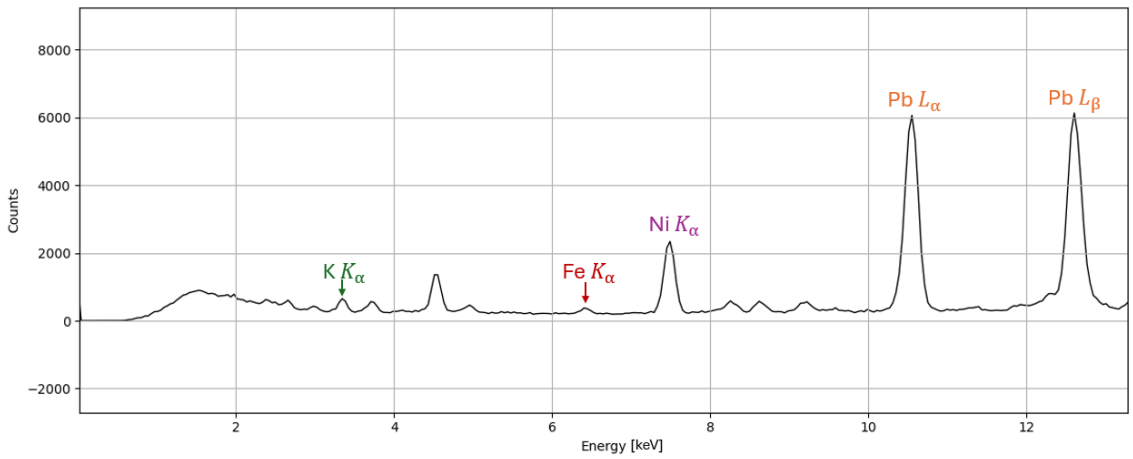

Figure 4.2: In vivo spectrum (Participant 024) visualized in PyMCA with relevant peaks labelled. Pb (orange) is present from the detector cap, Ni (purple) is from the detector, and Fe (red) and K (green) are from the participant.

It is interesting to note that the in vivo spectra differ from phantom spectra,

specifically regarding the presence of elements found in the human body. The in vivo spectra show small K, Cl, and Br peaks, demonstrated in Figure 4.3, that are not observed in phantom spectra. While interesting as it shows potential possibilities for the measurement system, this difference is not important and these elements do not need to be incorporated into phantoms for iron measurements as they do not interfere with the iron signal.

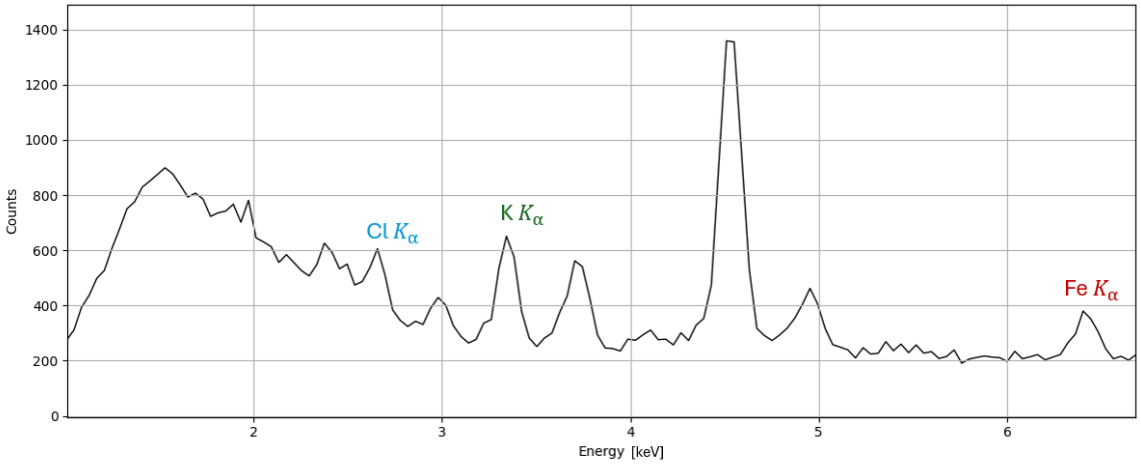

(a) Cl (blue) and K (green) peaks from an in vivo measurement, alongside Fe (red).

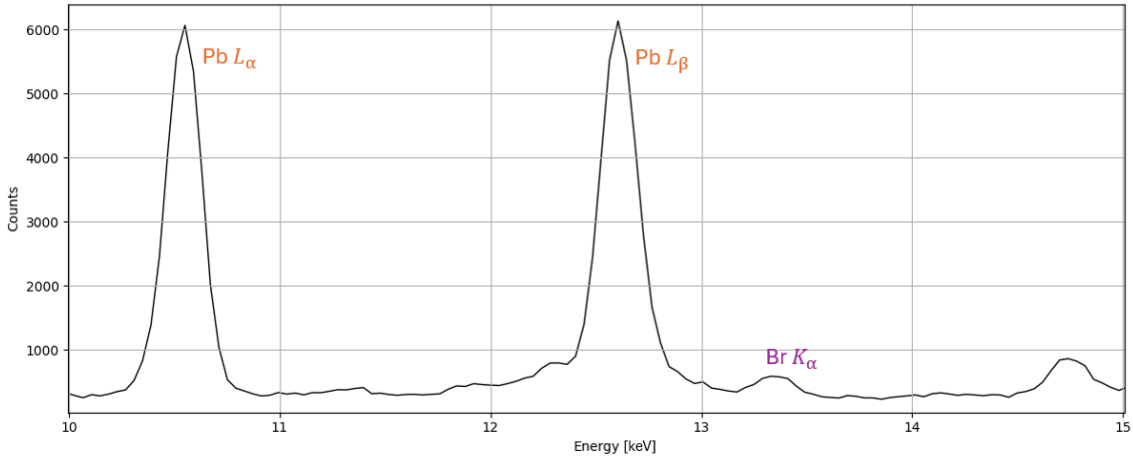

(b) Br (purple) peak from an in vivo measurement, alongside Pb (orange).

Figure 4.3: In vivo spectrum (Participant 024) visualized in PyMCA with relevant peaks labelled.

The results of the in vivo measurements are listed below in Table 4.1. As with previous phantom and animal skin measurements, the data were analyzed using the software OriginPro. The initial spectra data were converted to iron concentrations according to the calibration line in Figure 3.8. Therefore, Fe data was normalized to the Compton peak of the 22.1 keV Ag x-ray before being converted to an iron concentration based on the calibration line.

Participant ID	Age	Gender	Fe concentration [ppm]
001	24	F	12.5 ± 2.1
002	29	M	11.3 ± 2.4
003	27	M	13.3 ± 2.0
004	24	M	10.2 ± 1.9
005	24	M	5.3 ± 1.7
006	19	F	4.0 ± 2.0
007	23	F	6.9 ± 2.0
008	44	M	7.3 ± 2.5
009	18	F	3.5 ± 1.4
010	19	F	7.1 ± 1.7
011	18	F	8.0 ± 2.3
012	19	F	3.9 ± 2.1
013	24	M	14.0 ± 1.9
014	30	F	4.5 ± 2.1
015	60	F	10.9 ± 1.8
016	60	M	12.2 ± 1.8
017	43	M	9.9 ± 2.5
018	73	F	4.5 ± 2.1
019	76	F	17.1 ± 2.1
020	40	M	7.1 ± 2.0
021	30	M	4.5 ± 1.8
022	46	M	11.2 ± 1.7
023	65	M	13.2 ± 2.7
024	60	F	15.3 ± 1.6

Table 4.1: Results of in vivo measurements with calculated Fe concentrations for each participant. Uncertainty represents measurement uncertainty.

It is important to note that the first three participants in this study (Participants

001 - 003) were incorrectly instructed by the student researcher to place the dorsal side of their hand towards the detector, rather than the palm where the thenar eminence is located. This demonstrates the importance of having explicit protocol in place prior to measurement, and perhaps points towards the relevance of having a hand holder that is orientation-specific to avoid this mistake in the future.

It is also important to note that during one of the measurements (Participant 013), the fire alarm in the building went off and had to be evacuated for safety. As a result, the measurement did not go to completion of 1200 s but rather 999 s. This data was still analyzed for the purpose of this work because a ratio is taken of the counts collected, therefore differences in measurement time could be accounted for such that this data was still usable for this project. This data also introduces information regarding the feasibility of shorter measurement times.

4.5 Discussion

The main goal of this work was to investigate the feasibility of in vivo measurements of iron in the skin using this XRF system. The iron measurements (mean: 9.1 ppm with standard deviation ± 4.1 ppm) align with expected values from the literature, as well as the findings of pig skin measurements using this XRF system [39, 36]. To determine measurement feasibility, further analysis of the uncertainty data was performed.

To understand whether the system could measure iron levels in volunteers, tests were performed to determine whether individual measurement results could be considered detectable, i.e. significantly different from zero. Each measurement was divided by its uncertainty to calculate the difference from 0ppm in terms of the number of

uncertainties. A lookup table was used to calculate the significance of the difference (p-value). All measurements are different from zero at the 95% confidence level, and 20 of 24 measurements are different from zero at the 99% confidence level. The system was able to successfully measure iron levels in every participant in this small study population with 95% confidence, demonstrating feasibility of skin iron measurements in humans.

While effects of age and gender on iron concentrations were not main goals of this work, it was considered important to analyze whether age or gender influenced measurement feasibility. A plot of measurement uncertainty versus age is displayed in Figure 4.4. There appears to be no correlation between measurement uncertainty and age, suggesting that all age groups can be measured to the same level of precision.

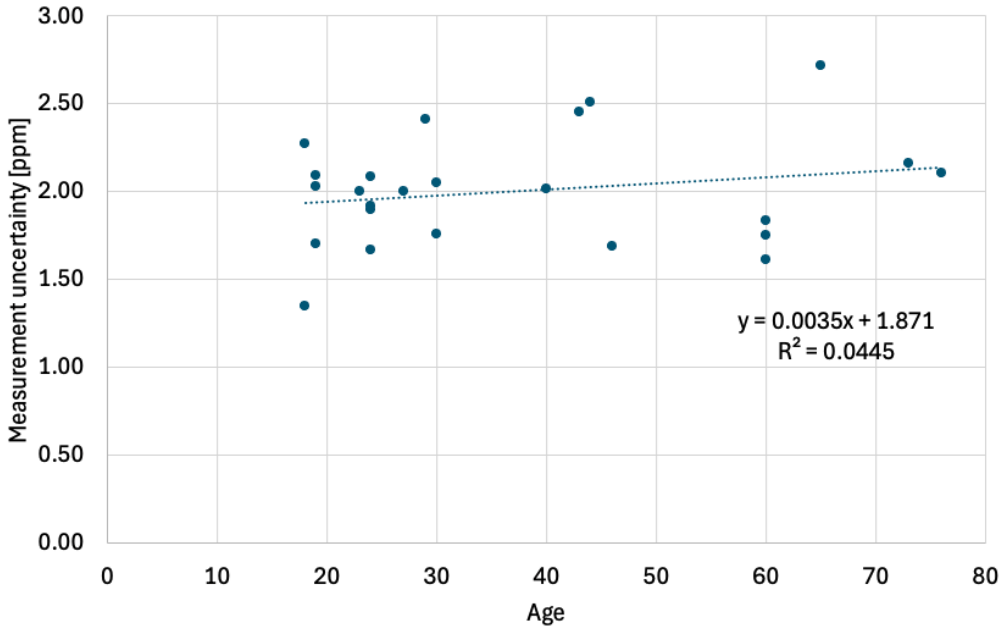

Figure 4.4: Comparison of iron measurement uncertainty versus participant age. The R^2 value is 0.04.

Regression analysis of iron measurement versus age is significant at the 95% confidence level, with a p-value for the correlation of 0.019. Iron has been found to accumulate with aging, so a correlation between iron concentration and age is not unexpected [40]. As shown in Figure 4.5, the correlation between iron measurement and age has an R^2 of 0.22. This suggests that age accounts for 22% of the variation in iron measurements as measured with this XRF system, with the rest of the variation being due to other unknown factors, some of which could be biological.

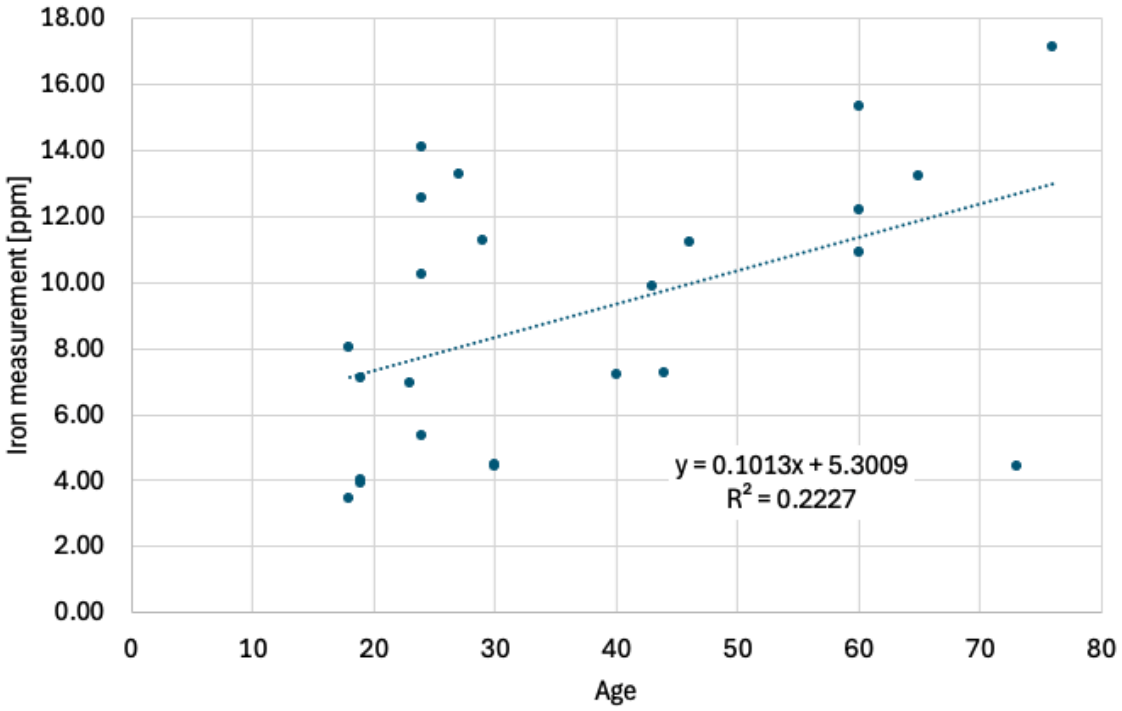

Figure 4.5: Comparison of iron measurement versus participant age. The R^2 value is 0.22.

Regarding gender, two histogram plots of measurement uncertainty values, one for each gender, are shown below in Figure 4.6. The graph suggests that the uncertainty in measurements of male participants is slightly higher, however when t-tested, the

data were not significantly different ($p = 0.4$). No statistically significant difference is presently observed in terms of XRF system performance for male compared to female participants.

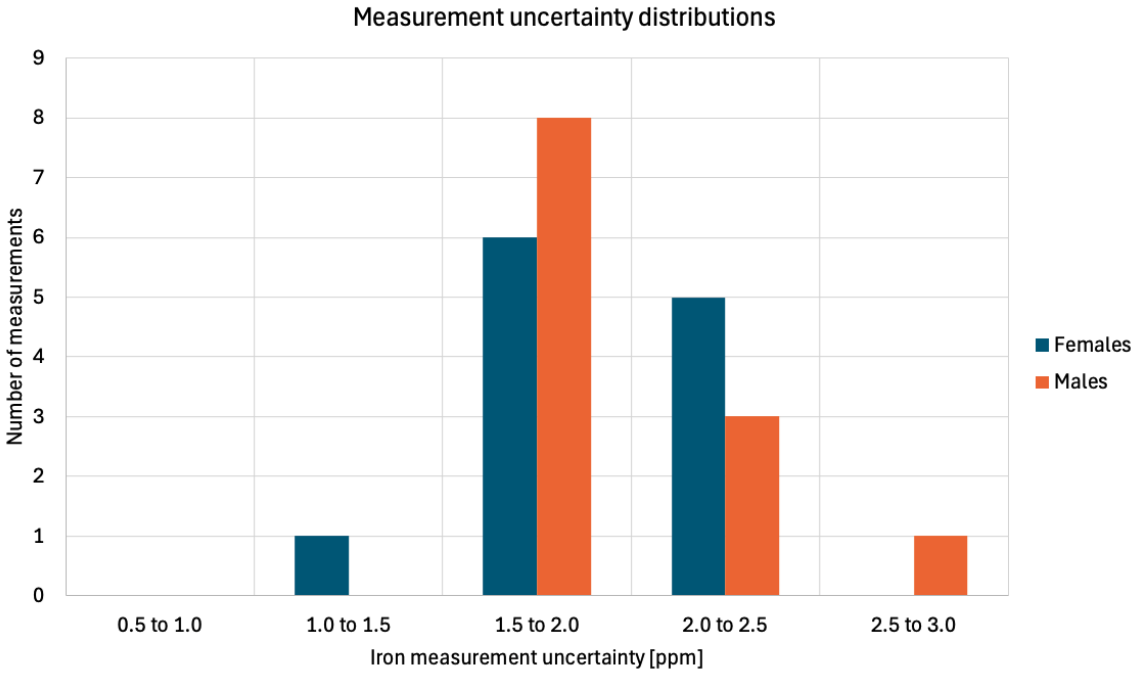

Figure 4.6: Comparison of iron measurement uncertainty versus participant gender.

In terms of measured levels of skin iron as determined by this XRF system, no statistically significant difference in iron levels is observed between males and females when a t-test is performed ($p = 0.23$). This suggests that male and female participants can be measured equally well with this XRF system.

Both the median and mean in vivo measurement uncertainty (σ) are 2.0 ppm for the study population. The 'in vivo detection limit' is therefore 4.0 ppm, as it is 2σ for a >95% confidence level, as outlined in Equation 2.3.3. This suggests that on average, the system can detect skin iron levels above 4.0 ppm with 95% confidence. For clinical use where 99% confidence levels may be preferred, the 3σ value of 6.0

ppm would possibly be used instead. The average measured iron level of the study population was 9.1 ppm with a standard deviation of 4.1 ppm. The standard deviation is approximately double the average measurement uncertainty obtained in phantoms. This suggests that there are variations other than radiation statistical uncertainty contributing to variance in vivo, which is expected due to human variation in iron levels, even among a normal population.

To determine a 'high' iron level based on these data, the standard deviation in the normal distribution of iron measurements (4 ppm) and the average individual measurement uncertainty (2 ppm) were summed in quadrature to obtain the uncertainty of the difference between an individual iron measurement and the average study population. A measurement more than twice this uncertainty higher than the average population would then be considered higher than 'normal': $2\sigma = 2\sqrt{4 \text{ ppm}^2 + 2 \text{ ppm}^2} = 8.9$ ppm.

Then, an iron level higher than 'normal' would be considered to be: $8.9 + 9.1 = 18.0$ ppm. Conversely, a low iron level would be calculated as: $9.1 - 8.9 = 0.2$ ppm. While this XRF system is thus highly likely to be able to detect patients with 'high iron', it cannot presently identify low iron levels, as this cannot readily be differentiated from zero. However, the XRF system can currently distinguish between 'normal' and 'elevated' iron levels when an individual measurement is 8.9ppm higher than the average.

Regarding the practicality of in vivo measurements, variation and thus differences in measurement uncertainty between participants was observed with respect to the hand holder. The detector's placement relative to the window of the hand holder was influenced by the location of the palm of the hand once it was secured into the

hand holder. If the participant had larger hands, then securing their hand may have led to their palmar tissue entering the window of the hand holder; then, the detector would need to be moved backwards to maintain the same distance from the detector to the hand. However, when the back of the hand was measured, the dorsal tissue did not experience the same expansion into the window of the hand holder. The flatter surface present on the dorsal side of the hand may have led to better measurements. This would need to be explored further in a future study, as no present literature discusses measuring the dorsal side of the hand for XRF skin iron measurements. For the purposes of this XRF device, this may be an advantageous measurement site.

4.6 Limitations

Measuring the back of the hand as opposed to the front could demonstrate iron differences due to varying epidermal thicknesses on each side, as mentioned in Chapter 1.4.2. Because the data from the first three participants were still included in all analysis, this does introduce hetereogeneity into the data which must be noted. However, iron distribution in the epidermis is not uniform. Most iron is thought to be present in the basal layer, therefore a thicker epidermis may result in different iron measurements due to the x-rays penetrating into the dermis.

Another limitation of this study is that data on race and ethnicity were not collected. This data would be relevant to determine how skin tone might affect the feasibility of using this XRF device. In future in vivo studies, it would be beneficial to collect this information to determine if there are differences in device performance across the range of skin tones that exist.

For future work, it would be beneficial to investigate the scatter introduced with

the hand holder. This would be important to investigate due to hand tissue entering the window of the hand holder. This investigation could be done through Monte Carlo simulation, adapting to previous work done by Bangash *et al.* [36]. Alternative means of improving the system include a redevelopment of the hand holding device, such that scatter can be reduced. This could be done through widening the window where the detector is placed, or orienting the detector in a different way such as from above, so that the hand does not need to be secured in the anterior-posterior direction aside from resting on a table. Alternatively, the current hand holder design could be used but printed at 100% infill rather than 20%. Unfortunately, this was not feasible with the 3D-printer that was used for this iteration of the hand holder due to the limitation of using one roll of filament at a time. This option could be done with another 3D-printer that allows multiple rolls of filament to be loaded at the start of a print. Printing at a higher infill percentage would increase photon absorption to reduce scatter.

4.7 Conclusion

The work in this Chapter points towards the feasibility of using this ^{109}Cd-based XRF device for in vivo measurements. A reasonable measurement time of 1200 s was used, which was possible due to hand restraint to avoid participant motion throughout the duration of the measurement. Calculated iron concentrations of the 24 participants aligned with literature and previous results from pig and rat skin measurements. Analysis of the measurement uncertainty values suggested that in vivo measurements are feasible, and age and gender do not influence measurement precision. While the device can measure normal and elevated iron levels, it cannot yet measure low iron

levels. Future work is recommended to investigate the accuracy of this device and work towards low iron measurement capabilities. However, the system can now be moved to the next phase of in vivo measurement studies. The system should be tested for its ability to measure the skin iron levels of patients with iron overload disease, and its ability to distinguish these levels from 'normal' levels.

4.8 Chapter summary

Overall, the findings of this work demonstrate preliminary successful use of this system for in vivo measurements of skin iron when measuring healthy participants. The data collected from 24 participants resulted in an average iron concentration of 9.1 with a measurement uncertainty of 2.0 ppm. Of the 24 participants, 21 were measured at the thenar eminence site while 3 were measured on the dorsal side of the hand. 12 female and 12 male participants in the age range of 18 to 76, mean age 37 with standard deviation ± 19 years, were recruited. Interestingly, the spectra collected also revealed the presence of K, Cl, and Br which differed compared to the phantoms that were measured previously. The in vivo detection limit was 4.0ppm, and measurement uncertainty analysis revealed that all measurements in this small study population are confident to the 95% level. No precision differences were observed across age and gender, suggesting that in vivo measurements are feasible using this XRF device.

This study revealed many improvements and adjustments that should be considered for the use of this XRF system moving forward. Notably, a new hand holder device could be developed. Potential improvements include the development of an orientation-specific design that ensures the correct placement of the hand during measurements. This can minimize the potential for incorrect hand orientation such as

what was observed during this study for 3 participants. Furthermore, it would be beneficial to consider a new design that does not introduce the possibility for tissue to extend into the detector area. As discussed in Chapter 3.4, depth effects are observed when samples are placed within the detector area, likely due to increased scatter. Because of this, a new design that minimizes scatter could be beneficial to improve consistency across measurements.

Once methodology improvements are made, the next step of this work would be to compare iron levels measured by this XRF system to measurements from a current standard such serum ferritin measurements. This would provide valuable information regarding the accuracy and reliability of these measurements for in vivo purposes. Further, it would be beneficial to evaluate the ability of this device to distinguish elevated from 'normal' iron levels.

Chapter 5

Conclusion and Future Work

This work investigated the feasibility of using a ^{109}Cd-based XRF system for in vivo measurements of iron in the skin. While this device was previously used to measure phantoms and ex vivo rat and pig skin samples, human measurements had not been done until now.

The findings in this thesis demonstrate the viability of a radioisotope-based hand-held portable system for iron measurements in vivo. This presents the prospect of a low-dose XRF device for timely measurements of trace elements in the body. The 1200s measurement time was reasonable for participants, but required restraint of the hand through the developed hand holder jig. The measurement site of the thenar eminence was practical, and could be accessed easily on all participants. Therefore, clinical use of this device can be viewed as reasonable, practical, and feasible. The 'all-in-one' nature of this device further supports clinical use through the portability of the system. In spite of the lower count rate of the colder ^{109}Cd source, the results from the in vivo measurements demonstrated that it was feasible to use this

^{109}Cd-based XRF device for human measurements. The average calculated iron concentration of 9.1 was in line with the expected range for healthy individuals, and the in vivo detection limit of 4.0ppm suggests that normal to elevated iron levels can be measured with 95% confidence using this device. Furthermore, statistical analysis of measurement uncertainty data demonstrated successful use of this system for in vivo iron measurements, with no precision differences observed across age or gender. Therefore, it is concluded that the radioisotope-based XRF device makes in vivo measurements of iron feasible.

There are many avenues for future work. Using this XRF device, suggested future work includes further measurements with this system focusing on an assessment of device accuracy. For a future study, serum ferritin results could be compared to the results from this XRF device within a study population. This work would provide valuable information on the accuracy and reliability of this XRF device to measure iron in the body. Similarly, it would be beneficial to carry out experiments to evaluate the ability of the XRF system to differentiate between high and 'normal' levels of iron. Since the final goal of this work is clinical implementation of this system, this future work would provide insight into the adequacy of this device.

It would also be beneficial to perform repeat measurements on participants to observe the reproducibility of these results. However, a major challenge facing this work would be the dose to participants. Renewed dosimetry studies would need to be performed to understand the dose participants would receive. Alongside repeat measurements, it would be beneficial to determine if measurement times can be further shortened. This could be done by collecting spectra at 5-minute intervals throughout a 20-minute measurement. This would provide insight into the feasibility of using

shorter measurement times, through observing if 5-, 10-, or 15-minute measurements correlate or predict 20-minute measurements.

As the device cannot measure low iron levels at present, further improvement is required for complete clinical implementation. One way of achieving an improved MDL would be through increased x-ray fluence, which could be realized with a hotter radioactive source.

The ^{109}Cd source used in this project is unfortunately costly and difficult to source from Russia. As this work continues, the source will decay and eventually reach a point when it is no longer usable for this purpose. At present, any future work likely needs to be done sooner rather than later due to the lowering activity of the source. Further research could investigate alternative radioisotope-based XRF systems, such as ^{125}I which has been investigated previously in this lab group [41]. Although it has a shorter half-life, ^{125}I can be more easily attained, making it an alternative feasible option.

Ultimately, this work points towards the feasibility of using a ^{109}Cd-based XRF system for in vivo measurements of iron in the body. This presents a potential non-invasive alternative method of measuring iron concentration through a quick measurement of skin iron at the hand.

Bibliography

[1] F. Jawad, "Iron in the Human Body," pp. 332–334, 1996.

[2] N. Abbaspour, R. Hurrell, and R. Kelishadi, "Review on iron and its importance for human health," *Journal of Research in Medical Sciences : The Official Journal of Isfahan University of Medical Sciences*, vol. 19, pp. 164–174, Feb. 2014.

[3] A. Pietrangelo, "Hereditary hemochromatosis," *Biochimica et Biophysica Acta (BBA) - Molecular Cell Research*, vol. 1763, pp. 700–710, July 2006.

[4] W. Wang, M. A. Knovich, L. G. Coffman, F. M. Torti, and S. V. Torti, "Serum ferritin: Past, present and future," *Biochimica et Biophysica Acta (BBA) - General Subjects*, vol. 1800, pp. 760–769, Aug. 2010.

[5] D. C. P. Gupta, "Role of Iron (Fe) in Body," *IOSR Journal of Applied Chemistry*, vol. 7, no. 11, pp. 38–46, 2014.

[6] E. McLean, M. Cogswell, I. Egli, D. Wojdyla, and B. de Benoist, "Worldwide prevalence of anaemia, WHO Vitamin and Mineral Nutrition Information System, 1993-2005," *Public Health Nutrition*, vol. 12, pp. 444–454, Apr. 2009.

[7] S.-R. Pasricha, J. Tye-Din, M. U. Muckenthaler, and D. W. Swinkels, "Iron deficiency," *The Lancet*, vol. 397, pp. 233–248, Jan. 2021.

[8] F. Bermejo and S. García-López, "A guide to diagnosis of iron deficiency and iron deficiency anemia in digestive diseases," *World Journal of Gastroenterology : WJG*, vol. 15, pp. 4638–4643, Oct. 2009.

[9] M. L. Parker, S. Storm, M. Sholzberg, P. M. Yip, and D. R. Beriault, "Revising Ferritin Lower Limits: It's Time to Raise the Bar on Iron Deficiency," *The Journal of Applied Laboratory Medicine*, vol. 6, pp. 765–773, Apr. 2021.

[10] P. C. Adams, "Epidemiology and diagnostic testing for hemochromatosis and iron overload," *International Journal of Laboratory Hematology*, vol. 37, no. S1, pp. 25–30, 2015. _eprint: https://onlinelibrary.wiley.com/doi/pdf/10.1111/ijlh.12347.

[11] K. J. Allen, L. C. Gurrin, C. C. Constantine, N. J. Osborne, M. B. Delatycki, A. J. Nicoll, C. E. McLaren, M. Bahlo, A. E. Nisselle, C. D. Vulpe, G. J. Anderson, M. C. Southey, G. G. Giles, D. R. English, J. L. Hopper, J. K. Olynyk, L. W. Powell, and D. M. Gertig, "Iron-Overload–Related Disease in *HFE* Hereditary Hemochromatosis," *New England Journal of Medicine*, vol. 358, pp. 221–230, Jan. 2008.

[12] C. C. Hsu, N. H. Senussi, K. Y. Fertrin, and K. V. Kowdley, "Iron overload disorders," *Hepatology Communications*, vol. 6, no. 8, pp. 1842–1854, 2022. _eprint: https://onlinelibrary.wiley.com/doi/pdf/10.1002/hep4.2012.

[13] E. Poggiali, E. Cassinerio, L. Zanaboni, and M. D. Cappellini, "An update on iron chelation therapy," *Blood Transfusion*, vol. 10, pp. 411–422, Oct. 2012.

[14] C. Thomas and L. Thomas, "Biochemical Markers and Hematologic Indices in the Diagnosis of Functional Iron Deficiency," *Clinical Chemistry*, vol. 48, pp. 1066–1076, July 2002.

[15] A. Dignass, K. Farrag, and J. Stein, "Limitations of Serum Ferritin in Diagnosing Iron Deficiency in Inflammatory Conditions," *International Journal of Chronic Diseases*, vol. 2018, no. 1, p. 9394060, 2018. _eprint: https://onlinelibrary.wiley.com/doi/pdf/10.1155/2018/9394060.

[16] I. Cavill, "Iron status as measured by serum ferritin: The marker and its limitations," *American Journal of Kidney Diseases*, vol. 34, pp. s12–s17, Oct. 1999.

[17] D. Hernando, Y. S. Levin, C. B. Sirlin, and S. B. Reeder, "Quantification of liver iron with MRI: State of the art and remaining challenges," *Journal of Magnetic Resonance Imaging*, vol. 40, pp. 1003–1021, Nov. 2014.

[18] N. F. Olivieri and G. M. Brittenham, "Iron-Chelating Therapy and the Treatment of Thalassemia," *Blood*, vol. 89, pp. 739–761, Feb. 1997.

[19] D. C. Rockey, S. H. Caldwell, Z. D. Goodman, R. C. Nelson, and A. D. Smith, "Liver biopsy†," *Hepatology*, vol. 49, pp. 1017–1044, Mar. 2009.

[20] J.-P. Villeneuve, M. Bilodeau, R. Lepage, J. Côté, and M. Lefebvre, "Variability in hepatic iron concentration measurement from needle-biopsy specimens," *Journal of Hepatology*, vol. 25, pp. 172–177, Aug. 1996.

[21] A. K. V, P. S. Rao, S. Adappa, P. Balanthimogru, and C. Mahabala, "Correlation between serum ferritin and bone marrow iron stores," *Tropical Doctor*, vol. 47, pp. 217–221, July 2017.

[22] J. Martí, E. Antón, and C. Valentí, "Complications of bone marrow biopsy," *British Journal of Haematology*, vol. 124, no. 4, pp. 557–558, 2004. _eprint: https://onlinelibrary.wiley.com/doi/pdf/10.1046/j.1365-2141.2003.04799.x.

[23] Y. Gandon, D. Olivié, D. Guyader, C. Aubé, F. Oberti, V. Sebille, and Y. Deugnier, "Non-invasive assessment of hepatic iron stores by MRI," *The Lancet*, vol. 363, pp. 357–362, Jan. 2004. Publisher: Elsevier.

[24] C. T. Quinn and T. G. St Pierre, "MRI Measurements of Iron Load in Transfusion-Dependent Patients: Implementation, Challenges, and Pitfalls: Iron Load and Magnetic Resonance Imaging," *Pediatric Blood & Cancer*, vol. 63, pp. 773–780, May 2016.

[25] A. Dwivedi, N. Agarwal, L. Ray, and A. K. Tripathi, eds., *Skin Aging & Cancer: Ambient UV-R Exposure*. Singapore: Springer Singapore, 2019.

[26] J. A. Wright, T. Richards, and S. K. S. Srai, "The role of iron in the skin and cutaneous wound healing," *Frontiers in Pharmacology*, vol. 5, July 2014. Publisher: Frontiers.

[27] M. Asano, K. Yamasaki, T. Yamauchi, T. Terui, and S. Aiba, "Epidermal iron metabolism for iron salvage," *Journal of Dermatological Science*, vol. 87, pp. 101–109, Aug. 2017.

[28] D. Lintzeri, N. Karimian, U. Blume-Peytavi, and J. Kottner, "Epidermal thickness in healthy humans: a systematic review and meta-analysis," *Journal of the European Academy of Dermatology and Venereology*, vol. 36, no. 8, pp. 1191–1200, 2022. _eprint: https://onlinelibrary.wiley.com/doi/pdf/10.1111/jdv.18123.

[29] M. Mogensen, H. A. Morsy, L. Thrane, and G. B. E. Jemec, "Morphology and Epidermal Thickness of Normal Skin Imaged by Optical Coherence Tomography," *Dermatology*, vol. 217, pp. 14–20, June 2008. Num Pages: 7 Place: Basel, Switzerland Publisher: S. Karger AG.

[30] F. Meurens, A. Summerfield, H. Nauwynck, L. Saif, and V. Gerdts, "The pig: a model for human infectious diseases," *Trends in Microbiology*, vol. 20, pp. 50–57, Jan. 2012.

[31] R. Gorodetsky, E. Loewenthal, A. Goldfarb, and E. A. Rachmilewitz, "Non-Invasive Evaluation of Iron Load and Clearance in Patients with -Thalassemia[a]," *Annals of the New York Academy of Sciences*, vol. 612, pp. 568–572, Dec. 1990.

[32] M. J. Farquharson and D. A. Bradley, "The feasibility of a sensitive low-dose method for the *in vivo* evaluation of Fe in skin using K-shell x-ray fluorescence (XRF)," *Physics in Medicine and Biology*, vol. 44, pp. 955–965, Apr. 1999.

[33] M. Estevam and C. R. Appoloni, "Use of Portable X-ray Fluorescence (PXRF) In Vivo as an Alternative Technique for the Assessment of Iron Levels in Patients With Thalassemia and Hemochromatosis," *Health Physics*, vol. 104, pp. 132–138, Feb. 2013.

[34] A. Thompson, J. Kirz, D. Attwood, E. Fullikson, M. Howells, J. Kortright,

Y. Liu, and A. Robinson, *X-ray Data Booklet*. Lawrence Berkeley National Library: Center for X-ray Optics and Advanced Light Source, third ed., Sept. 2009.

[35] S. U. K. Bangash, F. E. McNeill, M. J. Farquharson, and D. R. Chettle, "Feasibility of a^{109} Cd-based portable XRF device for measuring skin iron concentration in anaemic and Thalassaemic patients," *Biomedical Physics & Engineering Express*, vol. 8, p. 065034, Nov. 2022.

[36] S. U. Bangash, F. E. McNeill, and M. J. Farquharson, "Investigation of the accuracy of a portable^{109} Cd XRF system for the measurement of iron in skin," *Biomedical Physics & Engineering Express*, vol. 10, p. 035032, May 2024.

[37] L. M. Bickley, E. Da Silva, D. R. Chettle, and F. E. McNeill, "An improved radioisotope-based X-ray fluorescence system for the *in vivo* measurement of bone strontium," *Journal of Analytical Atomic Spectrometry*, vol. 40, no. 4, pp. 1086–1097, 2025.

[38] E. Dao, "X-Ray Fluorescence Measurement of Iron Accumulation in Skin as a Surrogate Marker for Iron Levels in Critical Organs and Total Body Iron Burden," Master's thesis.

[39] R. Gorodetsky, J. Sheskin, and A. Weinreb, "Iron, Copper, and Zinc Concentrations in Normal Skin and in Various Nonmalignant and Malignant Lesions," *International Journal of Dermatology*, vol. 25, no. 7, pp. 440–445, 1986. _eprint: https://onlinelibrary.wiley.com/doi/pdf/10.1111/j.1365-4362.1986.tb03449.x.

[40] D. Mangan, "Iron: an underrated factor in aging," *Aging (Albany NY)*, vol. 13, pp. 23407–23415, Oct. 2021.

[41] B. Tang, "X-Ray Fluorescence Measurement of Skin Iron Concentration Using An I-125-Based System," Master's thesis.